Inorganic Chemistry

Article

pubs.acs.org/IC

Density Functional Study for the Bridged Dinuclear Center Based on a High-Resolution X-ray Crystal Structure of ba_3 Cytochrome *c* Oxidase from *Thermus thermophilus*

Wen-Ge Han Du and Louis Noodleman*

Department of Integrative Structural and Computational Biology, TPC15, The Scripps Research Institute, 10550 North Torrey Pines Road, La Jolla, California 92037, United States

Supporting Information

ABSTRACT: Strong electron density for a peroxide type dioxygen species bridging the Fe_{a3} and Cu_B dinuclear center (DNC) was observed in the high-resolution (1.8 Å) X-ray crystal structures (PDB entries 3S8G and 3S8F) of ba_3 cytochrome *c* oxidase (C*c*O) from *Thermus thermophilus*. The crystals represent the as-isolated X-ray photoreduced C*c*O structures. The bridging peroxide was proposed to arise from the recombination of two radiation-produced $HO^{\bullet}$ radicals formed either very near to or even in the space between the two metals of the DNC. It is unclear whether this peroxide species is in the O_2^{2-}, $O_2^{\bullet-}$, HO_2^-, or the H_2O_2 form and what is the detailed electronic structure and binding geometry including the DNC. In order to answer what form of this dioxygen species was observed in the DNC of the 1.8 Å X-ray C*c*O crystal structure (3S8G), we have applied broken-symmetry density functional theory (BS-DFT) geometric and energetic calculations (using OLYP potential) on large DNC cluster models with different Fe_{a3}−Cu_B oxidation and spin states and with O_2^{2-}, $O_2^{\bullet-}$, HO_2^-, or H_2O_2 in the bridging position. By comparing the DFT optimized geometries with the X-ray crystal structure (3S8G), we propose that the bridging peroxide is HO_2^-. The X-ray crystal structure is likely to represent the superposition of the Fe_{a3}^{2+}−(HO_2^-)−Cu_B^+ DNC's in different states (Fe^{2+} in low spin (LS), intermediate spin (IS), or high spin (HS)) with the majority species having the proton of the HO_2^- residing on the oxygen atom (O1) which is closer to the Fe_{a3}^{2+} site in the Fe_{a3}^{2+}−(HO−O)$^-$−Cu_B^+ conformation. Our calculations show that the side chain of Tyr237 is likely trapped in the deprotonated $Tyr237^-$ anion form in the 3S8G X-ray crystal structure.

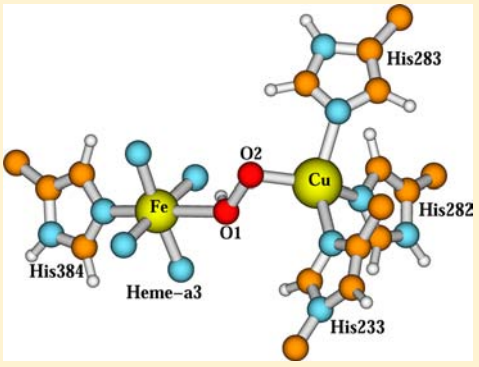

1. INTRODUCTION

Mitochondrial and bacterial respiration accounts for most of the global O_2 consumption and is the major source of energy via ATP synthesis in aerobic organisms.[1−5] Cytochrome *c* oxidase (C*c*O), located in the inner mitochondrial or bacterial membrane, is the terminal enzyme in the respiratory chain which binds O_2, reduces O_2 to H_2O, and pumps protons across the membrane.[6−9]

Four redox centers are present in C*c*O: (1) a homodinuclear Cu dimer in subunit II named Cu_A, which serves as the primary site of electron entry to C*c*O,[10,11] (2) a six-coordinate low-spin heme, which in the case of the aa_3 type of C*c*O is an a-heme (Fe_a) and in the case of the ba_3 type of C*c*O is a b-heme (Fe_b), (3) a variably coordinated heme-a (Fe_{a3}), which is more than 10 Å away from Fe_a or Fe_b, and (4) a single Cu ion named Cu_B, which is in the proximity of Fe_{a3} (∼5 Å). Heme-a (or b), heme-a_3, and Cu_B all locate in subunit I. The latter (heme Fe_{a3} and Cu_B) constitutes the dinuclear (or binuclear) center (DNC or BNC), which is the catalytic site where O_2 binds and is reduced.

Extensive experimental and theoretical studies on cytochrome oxidases in the past years have brought us a general picture about how O_2 reduction occurs in C*c*O's.[6−9,11−31] However, the precise structures of the C*c*O DNC in the intermediate states of the catalytic cycle, and even in the as-isolated oxidized state (Fe_{a3}^{3+}−Cu_B^{2+}) are still not clear.[6−8,32−42]

The electron density between Fe_{a3} and Cu_B in the as-isolated oxidized aa_3 type C*c*O's from *Paracoccus denitrificans* (*Pd*) and *Rhodobacter sphaeroides* (*Rs*) was originally interpreted as a H_2O and an OH^- ligand.[34,35] Recently, on the basis of the high-resolution X-ray crystal structures of the oxidized C*c*O's from *Pd* (PDB code 3HB3, 2.25 Å resolution)[39] and from bovine heart (PDB code 2ZXW, 1.95 Å resolution),[38] two research groups have independently proposed that a peroxide dianion (O_2^{2-}) bridges the Fe_{a3} and Cu_B in the DNC. Sakaguchi et al.[40] also reported a resonance Raman band (at 755 cm^{-1}) assignable to the O−O stretching mode of the bridging peroxide in the resting oxidized state of bovine heart C*c*O. Later, quantum-chemical calculations supported the idea that this bridging ligand in the resting oxidized DNC of bovine heart C*c*O is dioxygen (O_2), which may be reduced to superoxide ($O_2^{\bullet-}$) in the X-ray beam.[41] Discrepancies in the O−O bond length of this bridging ligand exist among these studies. The

Received: July 18, 2013
Published: November 21, 2013

O−O distance is refined to be 1.7 Å in the X-ray crystal structure (2ZXW),[38] which is significantly longer than those of model compounds with peroxide bridging between the metals.[43] This apparent O−O distance is most consistent with a physical mixture of different O−O-based and/or H_2O/OH^- species. An observed resonance Raman band at 755 cm^{-1} is consistent with an O−O distance of 1.50 Å.[40] Kaila's quantum-chemical DFT calculations show even shorter O−O distances of 1.29−1.32 Å for O_2 or $O_2^{\bullet-}$ bridges.[41] Therefore, further studies are still needed to clarify the form of the bridging ligand in the DNC of C*c*O.

In *Thermus thermophilus* (*Tt*), the ba_3 C*c*O has been crystallized under different conditions.[32,33,37,42] A water molecule was first reported to reside between Fe_{a3} and Cu_B in the DNC of the oxidized crystal structure (PDB entry 1XME, 2.3 Å resolution).[33] Later it was discovered that this structure actually represents the X-ray radiation reduced enzyme.[37] Recently, the wild-type (PDB code 3S8F) and the A120F mutant (PDB code 3S8G) X-ray crystal structures of the ba_3 C*c*O from *Tt* in a lipidic cubic phase (LCP) environment were obtained by Tiefenbrunn et al. at 1.8 Å resolution.[42] Similar to the bovine heart C*c*O (2ZXW),[38] strong electron density for a pair of bonded atoms bridging Fe_{a3} and Cu_B was also observed in 3S8F and 3S8G, which was best modeled as peroxide with a O−O distance of 1.52 Å.[42] Proton positions are not directly seen, but the protonation state can have important indirect effects on structures, properties, and reactions. As indicated in ref 42, the crystals were formed from the as-isolated enzyme at room temperature, in which spectral properties showed that all the redox cofactors were oxidized. The crystals were exposed to X-rays only after freezing at ∼100 K. However, during collection of X-ray diffraction data, the metal sites were undoubtedly reduced.[42] It was suggested that the bridging peroxide might arise from the recombination of two radiation produced $HO^{\bullet}$ radicals formed either very near to or even in the space between the two metals of the DNC.[42]

The wild-type (3S8F) and the A120F mutant (3S8G) X-ray crystal structures of C*c*O from *Tt* are almost identical (total RMSD ∼0.29 Å),[42] while 3S8G has a better defined electron density with lower *B* factors; therefore, the analysis presented in ref 42 focused on 3S8G. Since it is still an open question whether the bridging species seen in the DNC of 3S8G is O_2^{2-}, $O_2^{\bullet-}$, HO_2^-, or H_2O_2, in the current paper, we try to find a well-justified answer by performing density functional theory (DFT) calculations on the quantum cluster models of the 3S8G DNC, using OLYP potential.[44,45]

2. DNC OF THE 3S8G X-RAY CRYSTAL STRUCTURE OF THE BA_3 CCO FROM *TT*

The major components of the DNC observed in 3S8G are shown in Figure 1. O1 and O2 are the two oxygen atoms proposed to be peroxide. The Fe−O1, O1−O2, and Cu−O2 distances are 2.39, 1.52, and 2.25 Å, respectively.[42] Two water molecules HOH604 and HOH608 above O1−O2 are also found in the center, which are unique for this *Tt* C*c*O X-ray crystal structure. Note that there is an inconsistency in labeling the water molecules between ref 42 and the 3S8G.pdb file. HOH604 and HOH608 are given in 3S8G.pdb, while in ref 42 they are described as HOH165 and HOH65, respectively. In the current paper, we label the water molecules in our cluster models on the basis of the file 3S8G.pdb. HOH608 hydrogen bonds with the carbonyl of Gly232 (O···O distance 3.12 Å) and with HOH604 (O···O distance 2.64 Å) and is 3.01 Å above O2.

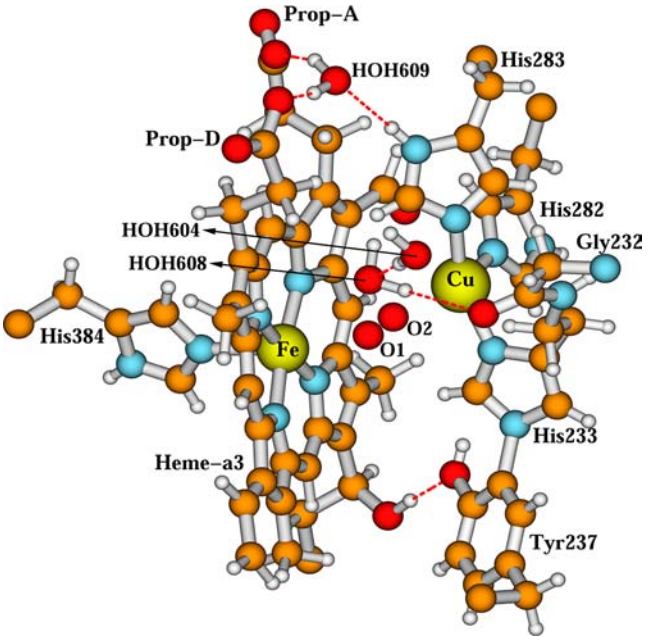

Figure 1. Heme-a_3 and Cu_B dinuclear center (DNC) observed in the ba_3 C*c*O X-ray crystal structure 3S8G from *Tt*.

As is well-known, in the DNC, Fe_{a3} has one histidine ligand (His384) and Cu_B has three histidine ligands: His233, His282, and His283. Figure 1 also shows the covalent linkage between Tyr237 and His233, a linkage which is common to all C*c*O's but otherwise unknown in metalloenzymes. HOH609 has hydrogen-bonding interactions with the two propionate carboxylate groups (prop-A and prop-D) and also with the His283 side chain. A water molecule in this position was also found in other C*c*O X-ray crystal structures.[33,35,38,39]

There is a water cluster above the DNC. The water molecules and the H-bonding residues above the DNC which are included in our quantum cluster models are shown in Figure 2. HOH609, the carboxylate groups of prop-A and prop-D, and part of the His283 side chain are also presented in Figure 2, in order to show how Figure 2 is connected with Figure 1.

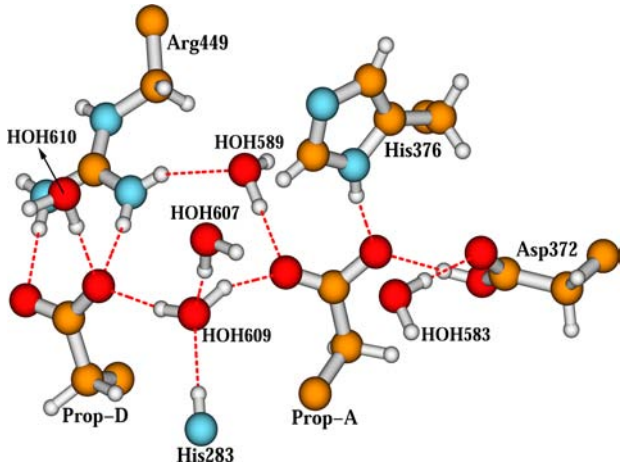

Figure 2. Water molecules and the H-bonding residue side chains above the DNC.

dx.doi.org/10.1021/ic401858s | *Inorg. Chem.* 2013, 52, 14072−14088

3. QUANTUM CLUSTER MODELS AND CALCULATION METHODS

The size of our models for quantum-chemical calculations is basically the combination of Figures 1 and 2. The starting *xyz* coordinates of our geometry optimization calculations are taken from 3S8G.pdb. The C_α atoms of Tyr237, His282, His283, Asp372, His376, and His384 are each replaced with a link H atom along the original $C_\beta-C_\alpha$ direction with the $C_\beta-H_{link}$ distance 1.09 Å. The C_γ of Arg449, N of Gly232, and C_{228} of the geranyl side chain of the a_3-heme are also replaced with a H_{link} atom. Initially the Tyr237 side chain is neutral in our models. However, in section 4.4.3 the deprotonated $Tyr237^-$ anion form is also used in our calculations. Depending on the protonation states of the O1−O2 species and of the Tyr237 side chain, the total atom number of our quantum clusters ranges from 204 to 206. Fee et al. used a similar but smaller (183−189 atoms) quantum cluster model to calculate 14 intermediate states of the DNC along the catalytic cycle.[11] The difference between the size of our model and theirs is that our model includes Gly232, HOH604, HOH608, and HOH610 but theirs does not.

Given the same oxidation states of Fe and Cu, different spin states of Fe (low, intermediate, or high spin) and different spin couplings (ferromagnetic or antiferromagnetic) between Fe and Cu will yield different geometric structures in the DNC and different energies. Therefore, choosing an accurate and yet practical functional to perform the DFT calculations on our large DNC models is very important. Recently, Vancoillie et al. tested the performance of CASPT2 (multiconfigurational perturbation theory) and a number of selected DFT functionals (B3LYP, B3LYP*, OLYP, BP86, TPSS, TPSSh, M06, and M06-L) for relative spin-state energetics of Fe^{2+} and Fe^{3+} heme models against available high-level coupled cluster singles and doubles (CCSD) results.[46] They have found that none of the tested density functionals consistently provides a better accuracy than CASPT2 for all their model complexes. However, the pure functional OLYP yields results similar to those for the hybrid functional B3LYP* or B3LYP. In addition, for their large heme models, the results of OLYP, B3LYP, and B3LYP* are reasonably close to the best estimate of the spin splittings, with errors typically ≤6 kcal mol^{-1}.[46] Radoń and Pierloot also investigated the performance of the CASSCF/CASPT2 approach and several DFT functionals (PBE0, B3LYP, BP86, and OLYP) in calculating the bonding of CO, NO, and O_2 molecules to two model heme systems.[47] They have found that the experimentally available binding energies are best reproduced by the CASPT2 method and with the OLYP functional. The CASSCF spin populations most closely correspond to the results obtained with the pure OLYP or BP86 rather than with the hybrid functionals.[47] Therefore, in the current study, we chose the OLYP functional to perform the geometry optimization and energetic calculations on our large DNC model clusters.

All calculations are performed using the Amsterdam Density Functional Package (ADF2012.01) with integration grid accuracy parameter 4.0.[48−50] Geometries are optimized within the conductor like screening (COSMO) solvation model.[51−54] Since both the cluster and the surrounding protein environment are quite polar and contain many water molecules, to be consistent with ref 11, a larger dielectric constant of a simple ketone (ε = 18.5) is applied to the environment in all COSMO calculations. The van der Waals radii 1.5, 1.4, 1.7, 1.52, 1.55, and 1.2 Å are used for atoms Fe, Cu, C, O, N, and H, respectively. The basic atoms are created using the "BASIS" key in ADF. The triple-ζ plus polarization (TZP) Slater-type basis set is applied to the Fe and Cu atoms and double-ζ plus polarization (DZP) basis set to other atoms. The inner cores of C(1s), N(1s), O(1s), Fe(1s,2s,2p), and Cu(1s,2s,2p) are treated by frozen core approximations. During the geometry optimizations, the positions of the H_{link} atoms on Tyr237, His282, His283, Asp372, His376, His384, and Arg449 and the C_α atom of Gly232 were fixed.

Models were established to see whether O_2^{2-}, $O_2^{\bullet-}$, HO_2^-, or H_2O_2 represents the peroxide species O1−O2 observed in the 3S8G crystal structure. The H-bonding pattern between O1−O2 and HOH608 (Figure 1) varies in different models depending on the protonation state of O1−O2.

(1) If a molecular oxygen lies between Fe_{a3}^{3+} and Cu_B^{2+} in the oxidized as-isolated DNC, when Fe_{a3}^{3+} and Cu_B^{2+} are radiation-reduced to Fe_{a3}^{2+} and Cu_B^{+}, the molecular oxygen may bind with the DNC and form the $Fe_{a3}^{3+}-O_2^{2-}-Cu_B^{2+}$ state. Since we only study the DNC in the current paper, we will simply use Fe and Cu to represent Fe_{a3} and Cu_B hereafter. Although the $Fe^{3+}-O_2^{2-}-Cu^{2+}$ state is thought by many researchers to be the intermediate state before the O−O bond cleavage in the C*c*O catalytic cycle,[11,29,30] it has not been observed experimentally.[6] Here, we geometry optimize the $Fe^{3+}-O_2^{2-}-Cu^{2+}$ DNC clusters in different spin states and compare them with the X-ray crystal structure. The starting structure of the $Fe^{3+}-O_2^{2-}-Cu^{2+}$ DNC model for geometry optimization is shown in Figure 3,

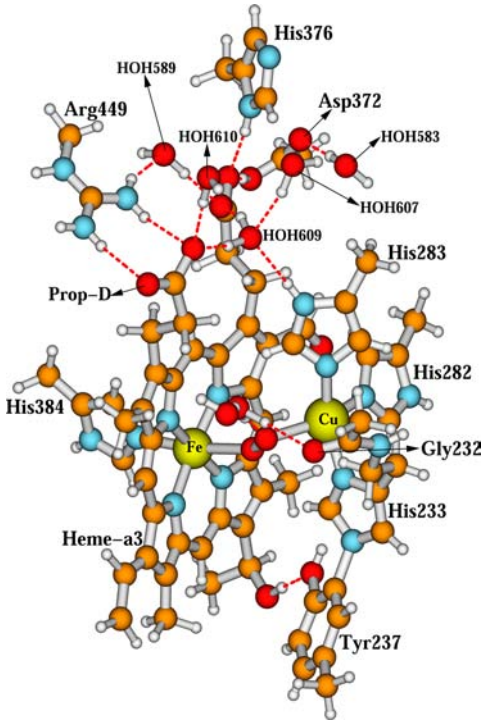

Figure 3. Initial structure of the $Fe^{3+}-O_2^{2-}-Cu^{2+}$, $Fe^{2+}-O_2^{\bullet-}-Cu^{+}$, and $Fe^{2+}-O_2^{2-}-Cu^{+}$ DNC model clusters. It is basically the combination of Figures 1 and 2 with H_{link} atoms. The central Fe−O1−O2−Cu portion is also shown in Figure 4 for the sake of clarity.

which is basically the combination of Figure 1 and Figure 2 containing the H_{link} atoms. The central Fe−O1−O2−Cu and the H-bonding patterns among O1−O2, HOH608, HOH604, and Gly232 are shown in Figure 4.

(2) If the molecular oxygen between Fe^{3+} and Cu^{2+} is also reduced in the X-ray beam and becomes superoxide ($O_2^{\bullet-}$), as Kaila et al. suggested for the aa_3 C*c*O from *Pd*,[38,41] then the DNC of the 3S8G crystal structure is in the $Fe^{2+}-O_2^{\bullet-}-Cu^{+}$ state. The starting structure of our $Fe^{2+}-O_2^{\bullet-}-Cu^{+}$ DNC models for geometry optimization is the same as the $Fe^{3+}-O_2^{2-}-Cu^{2+}$ state (see Figures 3 and 4).

(3) If the $O_2^{\bullet-}$ is $1e^-$ further reduced, then the DNC of the 3S8G crystal structure is in the $Fe^{2+}-O_2^{2-}-Cu^{+}$ state. Again, the starting geometry of our $Fe^{2+}-O_2^{2-}-Cu^{+}$ DNC models for geometry optimization is the same as the $Fe^{3+}-O_2^{2-}-Cu^{2+}$ state (see Figures 3 and 4).

(4) If HO_2^- represents O1−O2 in the DNC of the 3S8G crystal structure, the H-bonding interactions between O1−O2 and HOH608 are different in our calculations depending on whether the proton of the HO_2^- binds with O1 or O2. Figure 5 shows the central starting structure of our geometry optimization calculation for the $Fe^{2+}-(HO-O)^-Cu^{+}$ state, where the proton binds with O1. The rest of the structure is the same as in Figures 3 and 4. If the proton binds with O2, the starting conformation of the central $Fe^{2+}-(O-OH)^-Cu^{+}$ structure is shown in Figure 6, where the proton on O2 H-bonds with HOH608, which also H-bonds with HOH604 and the carbonyl of Gly232.

dx.doi.org/10.1021/ic401858s | *Inorg. Chem.* 2013, 52, 14072−14088

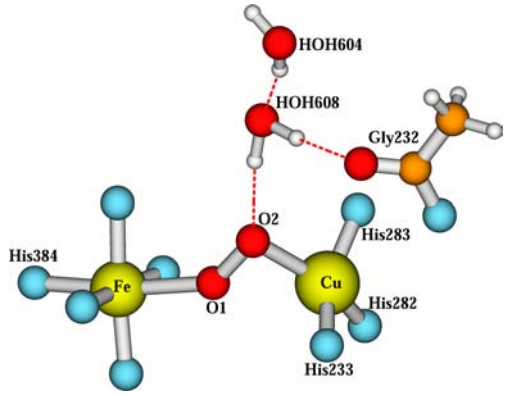

Figure 4. Detailed central Fe−O1−O2−Cu conformation of Figure 3 for the $Fe^{3+}-O_2^{2-}-Cu^{2+}$, $Fe^{2+}-O_2^{\bullet-}-Cu^{+}$, and $Fe^{2+}-O_2^{2-}-Cu^{+}$ DNC model clusters. The $Fe^{2+}-O_2^{\bullet-}-Cu^{+}$ model has one more electron than the $Fe^{3+}-O_2^{2-}-Cu^{2+}$ cluster and one less electron than the $Fe^{2+}-O_2^{2-}-Cu^{+}$ center.

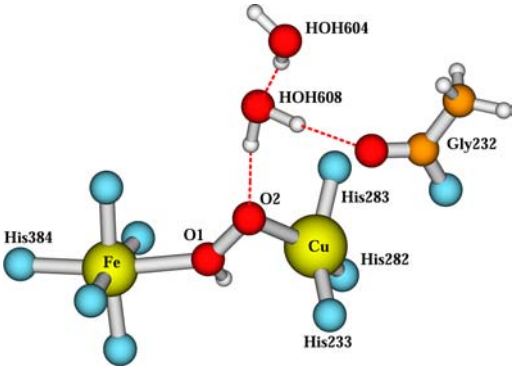

Figure 5. Central DNC of the starting conformation of the $Fe^{2+}-(HO-O)^{-}-Cu^{+}$ state for geometry optimization, where a proton binds with O1.

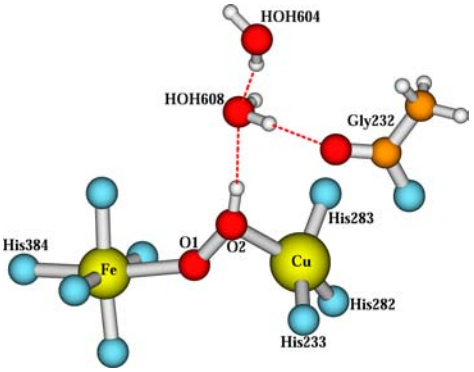

Figure 6. Central DNC of the starting conformation of the $Fe^{2+}-(O-OH)^{-}-Cu^{+}$ state, where a proton binds with O2 and H-bonds with HOH608.

(5) We will also study if the O1−O2 species is H_2O_2 in the 3S8G crystal structure. The starting conformation of the central portion of the $Fe^{2+}-HOOH-Cu^{+}$ DNC is shown in Figure 7, which is similar to Figure 6 but with O1 also protonated.

4. RESULTS AND DISCUSSION

4.1. $Fe^{3+}-O_2^{2-}-Cu^{2+}$ State Calculations. The Fe^{3+} site may exist as low spin (LS) with $S_{Fe} = {}^1/_2$, intermediate spin (IS) with $S_{Fe} = {}^3/_2$, or high spin (HS) with $S_{Fe} = {}^5/_2$. The Cu^{2+} has spin $S_{Cu} = {}^1/_2$. Further, the Fe^{3+} site may couple with the Cu^{2+} site ferromagnetically (F) with a total spin $S_{total} = S_{Fe} + S_{Cu}$ or antiferromagnetically (AF) with $S_{total} = S_{Fe} - S_{Cu}$. Therefore, there are six possible spin states for the $Fe^{3+}-O_2^{2-}-Cu^{2+}$ DNC model: $Fe^{3+,LS}-O_2^{2-}-Cu^{2+}(F)$, $Fe^{3+,LS}-O_2^{2-}-Cu^{2+}(AF)$, $Fe^{3+,IS}-O_2^{2-}-Cu^{2+}(F)$, $Fe^{3+,IS}-O_2^{2-}-Cu^{2+}(AF)$, $Fe^{3+,HS}-O_2^{2-}-Cu^{2+}(F)$, and $Fe^{3+,HS}-O_2^{2-}-Cu^{2+}(AF)$. For instance, $Fe^{3+,LS}-O_2^{2-}-Cu^{2+}(F)$ means the low-spin Fe^{3+} site ferromagnetically couples with the Cu^{2+} site in the $Fe^{3+}-O_2^{2-}-Cu^{2+}$ model.

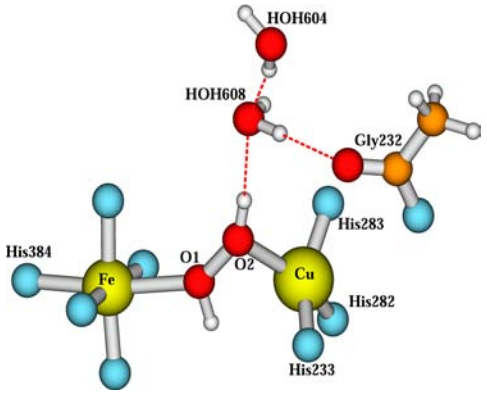

Figure 7. Central DNC of the starting conformation of the cluster in the $Fe^{2+}-HOOH-Cu^{+}$ state.

The AF-coupling spin state cannot be obtained directly from the normal DFT calculations. As in previous work,[55−61] we represent the AF spin-coupled state in DFT by a "broken-symmetry" (BS) state,[62−64] where a spin-unrestricted determinant is constructed in which the Fe^{3+} site has spin-up electrons as the majority spin and the Cu^{2+} site has majority spin-down electrons. Using OLYP potential, we have geometry optimized the $Fe^{3+}-O_2^{2-}-Cu^{2+}$ DNC cluster in the six spin states mentioned above. The main geometric, energetic, and Mulliken net spin population properties of these optimized structures are given in Table 1. Note that we failed to obtain an optimized geometry for the $Fe^{3+,IS}-O_2^{2-}-Cu^{2+}(AF)$ state. The $Fe^{3+,IS}-O_2^{2-}-Cu^{2+}(AF)$ and the $Fe^{3+,LS}-O_2^{2-}-Cu^{2+}(F)$ state have the same $S_{total} = 1$. Since the $Fe^{3+,LS}-O_2^{2-}-Cu^{2+}(F)$ state is much lower in energy, starting from the $Fe^{3+,IS}-O_2^{2-}-Cu^{2+}(AF)$ state the geometry optimization led to the $Fe^{3+,LS}-O_2^{2-}-Cu^{2+}(F)$ state. Therefore, we performed an $Fe^{3+,IS}-O_2^{2-}-Cu^{2+}(AF)$ state single-point energy calculation at the $Fe^{3+,IS}-O_2^{2-}-Cu^{2+}(F)$ optimized geometry. The $Fe^{3+,IS}-O_2^{2-}-Cu^{2+}(AF)$ single-point energy is very close to the $Fe^{3+,IS}-O_2^{2-}-Cu^{2+}(F)$ energy, about 2 kcal mol^{-1} higher than the F-coupled state.

The net spin populations from Mulliken population analysis are the main indication of the high-, intermediate-, or low-spin character of the Fe^{3+} site. In the ideal ionic limit, the net unpaired spin populations are 5, 3, and 1 for the HS, IS, and LS Fe^{3+} sites, respectively, and the net unpaired spin population for Cu^{2+} is 1. However, because of the metal−ligand covalency, the calculated net spin magnitudes for the Fe^{3+} and Cu^{2+} sites are smaller than their corresponding ionic limits. Our calculated net spins on Fe^{3+} and Cu^{2+} show that we obtained the correct spin state for each cluster. O1 and O2 also have large net spin populations—showing some superoxide character, especially in the F-coupled states. The opposite signs for the spin densities in Table 1 indicate the AF coupling.

Our calculations show that these optimized $Fe^{3+}-O_2^{2-}-Cu^{2+}$ DNC clusters yield similar Cu−O2 distances (1.98−2.08 Å).

dx.doi.org/10.1021/ic401858s | Inorg. Chem. 2013, 52, 14072−14088

Table 1. Calculated Properties of the $Fe^{3+}-O_2^{2-}-Cu^{2+}$ DNC Model in Different Spin States Using OLYP Potential[a]

	geometry									RMSD[b]			net spin[c]			
state[d]	O1–O2	Fe–O1	Fe–N (H384)	Cu–O2	Cu–N (H233)	Cu–N (H282)	Cu–N (H283)	Fe···Cu	Fe–O1–O2	Fe–O1–O2–Cu	5-atom	8-atom	all	E^e	Fe	Cu	O1	O2
$Fe^{3+,LS}-O_2^{2-}-Cu^{2+}$(F)	1.33	1.87	2.19	2.08	2.14	2.12	2.18	4.60	125	−137	0.57	0.50	0.37	−33.50	0.88	0.25	0.41	0.46
$Fe^{3+,LS}-O_2^{2-}-Cu^{2+}$(AF)	1.34	1.82	2.29	2.07	2.19	2.13	2.12	4.40	121	−123	0.53	0.46	0.33	−32.83	0.80	−0.26	−0.15	−0.29
$Fe^{3+,IS}-O_2^{2-}-Cu^{2+}$(F)	1.30	2.44	2.36	2.02	2.14	2.02	2.11	4.85	121	−132	0.40	0.37	0.31	−25.80	2.33	0.31	0.71	0.67
$Fe^{3+,IS}-O_2^{2-}-Cu^{2+}$(AF)[f]														−23.60	2.24	−0.22	0.15	0.01
$Fe^{3+,HS}-O_2^{2-}-Cu^{2+}$(F)	1.28	2.87	2.17	2.08	2.13	2.09	2.10	5.33	125	−133	0.46	0.47	0.39	−26.58	3.84	0.28	0.80	0.74
$Fe^{3+,HS}-O_2^{2-}-Cu^{2+}$(AF)	1.34	1.96	2.53	1.98	2.13	2.09	2.14	4.48	125	−132	0.46	0.40	0.32	−26.69	3.82	−0.29	0.21	−0.09
av-xyz[g]	1.32	2.19	2.31	2.04	2.14	2.10	2.13	4.73	124	−131	0.44	0.40	0.33					
exptl X-ray 3S8G	1.52	2.39	2.22	2.25	1.95	2.03	1.98	4.92	140	−147								

[a]The properties include geometry (Å, deg), RMSD (Å), electronic energy (E, −27900 kcal mol^{-1}), and the Mulliken net spin polarizations for Fe^{3+}, Cu^{2+}, O1, and O2 atoms (Figure 4). [b]Three root-mean-square deviations (RMSD) are calculated between each OLYP optimized geometry and the 3S8G.pdb[42] Cartesian coordinates: (1) for the central five atoms (in column "5-atom") at the DNC Fe, N(His384), O1, O2, and Cu; (2) for eight atoms (in column "8-atom") at the DNC Fe, N(His384), O1, O2, Cu, N(His233), N(His282), and N(His283); (3) for all the heavy atoms in the DNC cluster (in column "all") but without water molecules. [c]The Mulliken net spin polarizations are the subtractions between the number of α-spin electrons and the number of β-spin electrons. [d]Abbreviations: LS, low spin; IS, intermediate spin; HS, high spin; F, ferromagnetically coupled; AF, antiferromagnetically coupled. [e]The sum of −27900 kcal mol^{-1} (see footnote [a]) and the value given in this column gives the ADF "total energies", which are defined relative to a sum of atomic fragments (spherical spin-restricted atoms). Consequently, the energies of all electronic isomers and geometric and/or proton shift tautomers can be compared directly. Electron affinities can be simply computed, but their physical interpretation is complicated with respect to the (unknown) redox potentials of aquated electrons at low temperatures. The energies given for the AF coupling states in this paper are broken-symmetry state energies. [f]This is an $Fe^{3+,IS}-O_2^{2-}-Cu^{2+}$(AF) state single-point energy calculation on the $Fe^{3+,IS}-O_2^{2-}-Cu^{2+}$(F) optimized geometry. Geometry optimization calculations failed to get an optimized $Fe^{3+,IS}-O_2^{2-}-Cu^{2+}$(AF) state structure but instead obtained the $Fe^{3+,LS}-O_2^{2-}-Cu^{2+}$(F) state. [g]This structure is obtained by averaging the Cartesian coordinates of all the optimized $Fe^{3+}-O_2^{2-}-Cu^{2+}$ DNC clusters.

However, different Fe^{3+} spin states yield very different Fe–O1 and Fe–N(His384) distances. When Fe^{3+} is LS, both Fe–O1 (1.82–1.87 Å) and Fe–N(His384) (2.19–2.29 Å) are short. As a result, the Fe···Cu distance is also short (4.40–4.60 Å), which is much shorter than the experimental value (4.92 Å). From Fe^{3+}-LS to Fe^{3+}-IS, both Fe–O1 and Fe–N(His384) distances are increased (to 2.44 and 2.36 Å, respectively). Although the energies of the $Fe^{3+,HS}-O_2^{2-}-Cu^{2+}$(F) and $Fe^{3+,HS}-O_2^{2-}-Cu^{2+}$(AF) states are almost the same, their conformations at the DNC are very different. In $Fe^{3+,HS}-O_2^{2-}-Cu^{2+}$(F), Fe^{3+} binds with N(His384) (2.17 Å) but dissociates from O1 (2.87 Å). In $Fe^{3+,HS}-O_2^{2-}-Cu^{2+}$(AF), however, Fe^{3+} binds with O1 (1.96 Å) but dissociates from N(His384) (2.53 Å). Their Fe···Cu distances are also very different (5.33 vs. 4.48 Å). All $Fe^{3+}-O_2^{2-}-Cu^{2+}$ models yield O1–O2 bond lengths much shorter (1.28–1.34 Å) than the experimental value (1.52 Å).

The $Fe^{3+,LS}-O_2^{2-}-Cu^{2+}$(F) and $Fe^{3+,LS}-O_2^{2-}-Cu^{2+}$(AF) states have almost the same energies and very similar geometries. The $Fe^{3+,IS}-O_2^{2-}-Cu^{2+}$(F), $Fe^{3+,HS}-O_2^{2-}-Cu^{2+}$(F), and $Fe^{3+,HS}-O_2^{2-}-Cu^{2+}$(AF) states are 6–7 kcal mol^{-1} higher in energy than the $Fe^{3+,LS}-O_2^{2-}-Cu^{2+}$(F) and $Fe^{3+,LS}-O_2^{2-}-Cu^{2+}$(AF) states. Therefore, if the DNC of the 3S8G X-ray crystal structure is in the $Fe^{3+}-O_2^{2-}-Cu^{2+}$ state, it is likely to stay in the $Fe^{3+,LS}-O_2^{2-}-Cu^{2+}$(F) or $Fe^{3+,LS}-O_2^{2-}-Cu^{2+}$(AF) state. However, considering the DFT calculation energy uncertainties (see section 4.4.2 and section 5), and potential kinetic barriers at low temperatures, if the Fe site of the as-isolated protein started in the high-spin state, it may be trapped as high spin after reduction and then become either intermediate spin or high spin after transferring an electron to O_2; therefore, we cannot absolutely eliminate the possibility of the existence of the $Fe^{3+,IS}-O_2^{2-}-Cu^{2+}$ and $Fe^{3+,HS}-O_2^{2-}-Cu^{2+}$ states in some scenarios.

To see how well these OLYP optimized clusters represent the X-ray crystal structure, we have calculated the root-mean-square deviations (RMSD) between each optimized geometry and the 3S8G.pdb[42] Cartesian coordinates. Three RMSD's are calculated for each structure. (1) Focusing on the metal sites and the dioxygen positions, the RMSD (in column "5-atom") is calculated for the central five atoms at the DNC: Fe, N(His384), O1, O2, and Cu. (2) The RMSD (in column "8-atom") is further computed for the eight atoms at the DNC: Fe, N(His384), O1, O2, Cu, N(His233), N(His282), and N(His283). (3) The RMSD (in column "all") is calculated for all heavy atoms (except the water molecules) in the cluster. All RMSD(all) values in Table 1 are smaller than 0.4 Å and are much smaller than the corresponding RMSD(5-atom) and RMSD(8-atom) values. Except for the $Fe^{3+,HS}-O_2^{2-}-Cu^{2+}$(F) state, the RMSD(8-atom) values are 0.03–0.07 Å smaller than the corresponding RMSD(5-atom) values. Therefore, the central 5-atom positions reveal the major deviation of the OLYP optimized $Fe^{3+}-O_2^{2-}-Cu^{2+}$geometries from the X-ray crystal structure.

With the lowest electronic energies, the $Fe^{3+,LS}-O_2^{2-}-Cu^{2+}$(F) and $Fe^{3+,LS}-O_2^{2-}-Cu^{2+}$(AF) states, however, have the largest RMSD(5-atom) values (0.57 and 0.53 Å). The RMSD(5-atom) values of the higher energy $Fe^{3+,IS}-O_2^{2-}-Cu^{2+}$ and $Fe^{3+,HS}-O_2^{2-}-Cu^{2+}$ states are 0.40–0.46 Å, which are also not small. While the fit of the $Fe^{3+,LS}-O_2^{2-}-Cu^{2+}$(AF) structure to the RMSD(5-atom or 8-atom) is not in good agreement with the 1.8 Å protein X-ray structure, this calculated structure does match well with the EXAFS distances

and DFT BP86 computed geometry for a synthetic $Fe^{3+}-O_2^{2-}-Cu^{2+}$ complex.[29,30]

If all these states were trapped in the crystal structure, the Cartesian coordinates obtained from the X-ray diffraction analysis should represent the superposition of the atom positions of all these states. For simplicity, we have calculated the average of the Cartesian coordinates of these optimized $Fe^{3+}-O_2^{2-}-Cu^{2+}$ structures and have given their DNC geometric parameters in Table 1. In comparison with experiment, this averaged structure ("av-*xyz*") also gives an O1–O2 distance that is too short. The RMSD(5-atom) value between this averaged structure and the X-ray crystal structure is 0.44 Å.

Considering the large discrepancies between the X-ray crystal structure and the calculated $Fe^{3+}-O_2^{2-}-Cu^{2+}$ structures at the DNC and the fact that the $Fe^{3+}-O_2^{2-}-Cu^{2+}$ state has not been clearly observed by spectroscopic or structural experiments, the $Fe^{3+}-O_2^{2-}-Cu^{2+}$ models are therefore unlikely to represent the DNC in the 3S8G crystal structure.

4.2. $Fe^{2+}-O_2^{\bullet-}-Cu^{+}$ State Calculations. The Fe^{2+} site may exist as low spin (LS) with $S_{Fe} = 0$, intermediate spin (IS) with $S_{Fe} = 1$, or high spin (HS) with $S_{Fe} = 2$. $O_2^{\bullet-}$ has spin $S_{O_2^{\bullet-}} = {}^1/_2$, and in theory Cu^+ has net spin $S_{Cu} = 0$. Therefore, when Fe^{2+} is in the IS or HS state, the Fe^{2+} site may be F-coupled (with $S_{total} = S_{Fe} + S_{O_2^{\bullet-}}$) or AF-coupled (with $S_{total} = S_{Fe} - S_{O_2^{\bullet-}}$) to $O_2^{\bullet-}$. Therefore, there are five possible spin states for the $Fe^{2+}-O_2^{\bullet-}-Cu^+$ DNC model: $Fe^{2+,LS}-O_2^{\bullet-}-Cu^+$, $Fe^{2+,IS}-O_2^{\bullet-}-Cu^+$(F), $Fe^{2+,IS}-O_2^{\bullet-}-Cu^+$(AF), $Fe^{2+,HS}-O_2^{\bullet-}-Cu^+$(F), and $Fe^{2+,HS}-O_2^{\bullet-}-Cu^+$(AF). Again, the AF-coupled states are represented by "broken-symmetry" states. The main geometric, energetic, RMSD, and Mulliken net spin population properties of the optimized $Fe^{2+}-O_2^{\bullet-}-Cu^+$ structures are given in Table 2.

The net spin populations show that the optimized structures also have $Fe^{3+}-O_2^{2-}-Cu^+$ and $Fe^{2+}-O_2^{2-}-Cu^{2+}$ electronic state character, in addition to $Fe^{2+}-O_2^{\bullet-}-Cu^+$, indicating a mixture of three valence states.

The O1–O2 bond lengths (1.35–1.38 Å) of the optimized $Fe^{2+}-O_2^{\bullet-}-Cu^+$ clusters are slightly longer than those in the $Fe^{3+}-O_2^{2-}-Cu^{2+}$ clusters but are still 0.14–0.17 Å shorter than the observed value (1.52 Å). All of the $Fe^{2+}-O_2^{\bullet-}-Cu^+$ states yield very short Fe···Cu (4.21–4.50 Å) distances and long Cu–N(His233) and Cu–N(His283) distances. Experimentally, the Fe–O1 distance (2.39 Å) is longer than the Fe–N(His384) distance (2.22 Å). This is the opposite of the optimized $Fe^{2+}-O_2^{\bullet-}-Cu^+$ structures: i.e. the Fe1–O1 (1.84–2.14 Å) distances are short but the Fe–N(His384) distances (2.55–2.83 Å) are very long. The His384 side chain dissociates from the Fe^{2+} site in all of the optimized $Fe^{2+}-O_2^{\bullet-}-Cu^+$ clusters.

The $Fe^{2+,LS}-O_2^{\bullet-}-Cu^+$ state has much lower energy (by ~10 kcal mol^{-1}) than the $Fe^{2+,IS}-O_2^{\bullet-}-Cu^+$ and $Fe^{2+,HS}-O_2^{\bullet-}-Cu^+$ states. Consequently, if $O_2^{\bullet-}$ did represent the dioxygen species in the 3S8G X-ray crystal structure, the DNC of the crystal structure would likely be in the $Fe^{2+,LS}-O_2^{\bullet-}-Cu^+$ state. The positions of the central eight atoms Fe, N(His384), O1, O2, Cu, N(His233), N(His282), and N(His283) in 3S8G.pdb[42] and in $Fe^{2+,LS}-O_2^{\bullet-}-Cu^+$ are compared in Figure 8. For the less probable case that $Fe^{2+,IS}-O_2^{\bullet-}-Cu^+$ and $Fe^{2+,HS}-O_2^{\bullet-}-Cu^+$ states coexist with the $Fe^{2+,LS}-O_2^{\bullet-}-Cu^+$ state, we also calculated the average of the *xyz* coordinates ("av-*xyz*" in Table 2) of all the optimized $Fe^{2+}-O_2^{\bullet-}-Cu^+$ geometries. In comparison with the experiment, this av-*xyz* also shows very short O1–O2, Fe–O1, and Fe···Cu distances and a very long Fe–N(His384) distance. The calculated RMSD(5-atom) value

Table 2. Calculated Properties of the $Fe^{2+}-O_2^{\bullet-}-Cu^+$ DNC Model in Different Spin States Using OLYP Potential[a]

	geometry									RMSD			net spin				
state	O1–O2	Fe–O1	Fe–N (H384)	Cu–O2	Cu–N (H233)	Cu–N (H282)	Cu–N (H283)	Fe···Cu	Fe–O1–O2	Fe–O1–O2–Cu	5-atom	8-atom	all	*E*	Fe	Cu	O1	O2
$Fe^{2+,LS}-O_2^{\bullet-}-Cu^+$	1.37	1.84	2.55	2.02	2.37	2.10	2.25	4.32	120	−124	0.49	0.46	0.38	−16.81	0.40	0.13	0.30	0.25
$Fe^{2+,IS}-O_2^{\bullet-}-Cu^+$(F)	1.35	2.14	2.60	1.99	2.32	2.09	2.20	4.50	134	−117	0.37	0.38	0.37	−6.77	2.16	0.22	0.60	0.48
$Fe^{2+,IS}-O_2^{\bullet-}-Cu^+$(AF)[b]														−5.06	2.08	−0.21	−0.06	−0.16
$Fe^{2+,HS}-O_2^{\bullet-}-Cu^+$(F)	1.38	1.98	2.83	1.99	2.29	2.10	2.20	4.27	127	−114	0.41	0.38	0.33	−7.00	3.83	0.22	0.50	0.37
$Fe^{2+,HS}-O_2^{\bullet-}-Cu^+$(AF)	1.37	1.94	2.83	1.95	2.27	2.08	2.25	4.21	118	−108	0.49	0.44	0.36	−4.70	3.63	−0.22	0.00	−0.27
av-*xyz*[c]	1.36	1.97	2.70	1.98	2.31	2.09	2.22	4.32	126	−115	0.42	0.40	0.36					
exptl X-ray 3S8G	1.52	2.39	2.22	2.25	1.95	2.03	1.98	4.92	140	−147								

[a]The properties include geometry (Å, deg), RMSD (Å), electronic energy (*E*, −28000 kcal mol^{-1}), and the Mulliken net spin polarizations for Fe^{2+}, Cu^+, O1, and O2 atoms (Figure 4). See footnotes b–e of Table 1. [b]This is an $Fe^{2+,IS}-O_2^{\bullet-}-Cu^+$(AF) state single-point energy calculation on the $Fe^{2+,IS}-O_2^{\bullet-}-Cu^+$(F) optimized geometry. Geometry optimization calculations failed to get an optimized $Fe^{2+,IS}-O_2^{\bullet-}-Cu^+$(AF) structure but instead obtained the $Fe^{2+,LS}-O_2^{\bullet-}-Cu^+$ state. [c]This structure is obtained by averaging the Cartesian coordinates of all the optimized $Fe^{2+}-O_2^{\bullet-}-Cu^+$ DNC clusters.

dx.doi.org/10.1021/ic401858s | Inorg. Chem. 2013, 52, 14072–14088

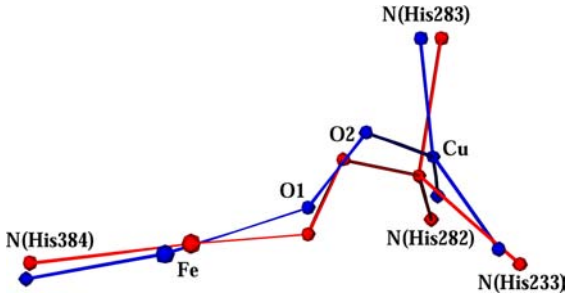

Figure 8. Comparison of the positions of Fe, N(His384), O1, O2, Cu, N(His233), N(His282), and N(His283) in the DNC's of 3S8G.pdb (blue) and $Fe^{2+,LS}-O_2^{\bullet-}-Cu^+$ (red). The RMSD between these two 8-atom structures is 0.46 Å (see Table 2).

for the optimized $Fe^{2+,LS}-O_2^{\bullet-}-Cu^+$ geometry and for av-*xyz* are large (0.49 and 0.42 Å, respectively). On the basis of these discrepancies, the $Fe^{2+}-O_2^{\bullet-}-Cu^+$ state is unlikely to represent the DNC of the 3S8G crystal structure.

4.3. $Fe^{2+}-O_2^{2-}-Cu^+$ State Calculations. Since Cu^+ has net spin $S_{Cu} = 0$, the $Fe^{2+}-O_2^{2-}-Cu^+$ cluster may exist in three kinds of spin states: $Fe^{2+,LS}$-O_2^{2-}-Cu^+, $Fe^{2+,IS}-O_2^{2-}-Cu^+$, and $Fe^{2+,HS}-O_2^{2-}-Cu^+$, depending on whether the Fe^{2+} site is LS, IS, or HS. The main geometric, energetic, RMSD, and Mulliken net spin population properties of the optimized $Fe^{2+}-O_2^{2-}-Cu^+$ structures are given in Table 3.

Although we set "spin-unrestricted" in our input files for geometry optimizations, we obtained the closed-shell $Fe^{2+,LS}-O_2^{2-}-Cu^+$ state, which has the lowest energy among the three possible spin states. For the alternative spin states, the net spin populations show that the optimized $Fe^{2+,IS}-O_2^{2-}-Cu^+$ and $Fe^{2+,HS}-O_2^{2-}-Cu^+$ states have significant Fe^+ and $O_2^{\bullet-}$ character as well.

In the X-ray crystal structure, the Fe−O1 (2.39 Å) distance is longer than both the Fe−N(His384) (2.22 Å) and Cu−O2 (2.25 Å) bond lengths. However, all optimized $Fe^{2+}-O_2^{2-}-Cu^+$ structures and their av-*xyz* values show very strong Fe−O1 binding. As a result, the Fe−O1 distances are all shorter than the corresponding Cu−O2 bond lengths, and all His384 side chains dissociate from the Fe^{2+} sites. The RMSD(5-atom) and RMSD(8-atom) values (0.43−0.55 Å) are not small. Therefore, the $Fe^{2+}-O_2^{2-}-Cu^+$ cluster also does not represent the DNC of the 3S8G X-ray crystal structure.

4.4. $Fe^{2+}-HO_2^{-}-Cu^+$ DNC Calculations. Now we study if HO_2^- represents the O1−O2 dioxygen species in the DNC of the 3S8G X-ray crystal structure and whether the proton resides on O1 or O2. As described above, the cluster is named as $Fe^{2+}-(HO-O)^-Cu^+$ (Figure 5) or $Fe^{2+}-(O-OH)^-Cu^+$ (Figure 6) if the proton binds with O1 or O2, respectively. Since we have found that the $Fe^{2+}-(HO-O)^-Cu^+$ DNC case is more complex, we present the $Fe^{2+}-(O-OH)^-Cu^+$ results first.

4.4.1. $Fe^{2+}-(O-OH)^-Cu^+$ DNC Calculations. The $Fe^{2+}-(O-OH)^-Cu^+$ (Figure 6) DNC has been geometry optimized in the following three spin states: $Fe^{2+,LS}-(O-OH)^-Cu^+$, $Fe^{2+,IS}-(O-OH)^-Cu^+$, and $Fe^{2+,HS}-(O-OH)^-Cu^+$. Their main calculated properties are given in Table 4. The central portions of the optimized $Fe^{2+,LS}-(O-OH)^-Cu^+$ and $Fe^{2+,IS}-(O-OH)^-Cu^+$ clusters are shown in Figures 9 and 10, respectively. The overall optimized geometry of the $Fe^{2+,HS}-(O-OH)^-Cu^+$ state is very similar to that of the $Fe^{2+,IS}-(O-OH)^-Cu^+$ state. The $Fe^{2+,LS}-(O-OH)^-Cu^+$ state is about 4−5 kcal mol^{-1} lower in energy than the $Fe^{2+,IS}-(O-OH)^-Cu^+$ and $Fe^{2+,HS}-(O-OH)^-Cu^+$ states.

Table 3. Calculated Properties of the $Fe^{2+}-O_2^{2-}-Cu^+$ DNC Model in Different Spin States Using OLYP Potential[a]

	geometry									RMSD			net spin			
state	O1−O2	Fe−O1	Fe−N (H384)	Cu−O2	Cu−N (H233)	Cu−N (H282)	Cu−N (H283)	Fe···Cu	Fe−O1−O2	Fe−O1−O2−Cu	5-atom	8-atom	all	E	Fe	Cu	O1	O2
$Fe^{2+,LS}-O_2^{2-}-Cu^+$	1.40	1.81	2.42	1.95	2.52	2.04	2.42	4.12	119	−116	0.55	0.48	0.36	−73.89	0.00	0.00	0.00	0.00
$Fe^{2+,IS}-O_2^{2-}-Cu^+$	1.39	1.83	2.39	1.99	2.35	2.08	2.30	4.24	120	−121	0.51	0.44	0.31	−71.90	0.66	0.12	0.27	0.18
$Fe^{2+,HS}-O_2^{2-}-Cu^+$	1.42	1.93	3.04	1.95	2.54	2.04	2.29	4.08	120	−117	0.47	0.45	0.39	−62.19	2.58	0.16	0.44	0.24
av-*xyz*[b]	1.40	1.86	2.62	1.96	2.47	2.05	2.34	4.15	120	−118	0.47	0.43	0.34					
exptl X-ray 3S8G	1.52	2.39	2.22	2.25	1.95	2.03	1.98	4.92	140	−147								

[a]The properties include geometry (Å, deg), RMSD (Å), electronic energy (E, −28000 kcal mol^{-1}), and the Mulliken net spin polarizations for Fe^{2+}, Cu^+, O1, and O2 atoms. See footnotes b−e of Table 1. [b]This structure is obtained by averaging the Cartesian coordinates of all the optimized $Fe^{2+}-O_2^{2-}-Cu^+$ DNC clusters.

dx.doi.org/10.1021/ic401858s | Inorg. Chem. 2013, 52, 14072−14088

Table 4. Calculated Properties of the Fe^{2+}−(O−OH)$^-$−Cu^+ (Figure 6) DNC Models in Different Spin States Using OLYP Potential[a]

state	geometry										RMSD			net spin		
	O1−O2	Fe−O1	Fe−N (H384)	Cu−O2	Cu−N (H233)	Cu−N (H282)	Cu−N (H283)	Fe···Cu	Fe−O1−O2	O···O (Y237)	Fe−O1−O2−Cu	5-atom	8- atom	all	E	Fe	Cu	O1	O2
$Fe^{2+,LS}$−(O−OH)$^-$−Cu^+	1.49	1.87	2.19	2.90	2.03	2.09	2.05	5.30	115	3.24	−127	0.59	0.54	0.35	−102.32	0.00	0.00	0.00	0.00
$Fe^{2+,IS}$−(O−OH)$^-$−Cu^+	1.47	1.99	2.69	3.33	2.03	2.09	2.06	5.09	119	3.30	−140	0.53	0.53	0.38	−98.48	2.21	0.00	0.35	0.06
$Fe^{2+,HS}$−(O−OH)$^-$−Cu^+	1.48	1.96	2.63	3.07	2.03	2.10	2.04	5.06	118	3.25	−134	0.48	0.33	0.33	−97.03	3.81	0.00	0.32	0.04
av-xyz[b]	1.41	1.94	2.50	3.08	2.03	2.10	2.05	5.15	120	3.26	−130	0.49	0.48	0.35					
exptl X-ray 3S8G	1.52	2.39	2.22	2.25	1.95	2.03	1.98	4.92	140	2.66	−147								

[a]The properties include geometry (Å, deg), RMSD (Å), electronic energy (E, −28000 kcal mol^{-1}), and the Mulliken net spin polarizations for Fe^{2+}, Cu^+, O1, and O2 atoms. See footnotes b−e of Table 1. [b]This structure is obtained by averaging the Cartesian coordinates of all the optimized Fe^{2+}−(O−OH)$^-$−Cu^+ DNC clusters.

Figure 9. Central portion of the DNC of the optimized $Fe^{2+,LS}$−(O−OH)$^-$−Cu^+ cluster, where a proton binds with O2.

Figure 10. Central portion of the DNC of the optimized $Fe^{2+,IS}$−(O−OH)$^-$−Cu^+ cluster, where a proton binds with O2. The optimized $Fe^{2+,HS}$−(O−OH)$^-$−Cu^+ structure is very similar to this.

The O1−O2 bond lengths (1.47−1.49 Å) of these three optimized Fe^{2+}−(O−OH)$^-$−Cu^+ structures are longer than those in the Fe^{3+}−O_2^{2-}−Cu^{2+}, Fe^{2+}−$O_2^{\bullet-}$−Cu^+, and Fe^{2+}−O_2^{2-}−Cu^+ model clusters and are very close to the experimental value (1.52 Å). Evidently, HO_2^- is better than O_2^{2-} and $O_2^{\bullet-}$ at representing the dioxygen species in the 3S8G crystal structure. However, other DNC geometric parameters of these three optimized structures are not consistent with the experiment. For instance, O2 dissociates from the Cu site in these models, and meanwhile, the Fe−O1 bond lengths are much shorter (by 0.40−0.52 Å) than the observed value (2.39 Å). In $Fe^{2+,IS}$−(O−OH)$^-$−Cu^+ and $Fe^{2+,HS}$−(O−OH)$^-$−Cu^+ clusters, the His384 side chain dissociates from the Fe site. The RMSD(5-atom) value for the optimized $Fe^{2+,LS}$−(O−OH)$^-$−Cu^+ state is 0.59 Å, which is so far the largest among all the calculated RMSD(5-atom) values. Therefore, although the O1−O2 bond length is consistent with experiment, the Fe^{2+}−(O−OH)$^-$−Cu^+ state alone is unlikely to represent the DNC structure in 3S8G.pdb.

4.4.2. Fe^{2+}−(HO−O)$^-$−Cu^+ DNC Calculations. The geometry of the Fe^{2+}−(HO−O)$^-$−Cu^+ (Figure 5) DNC has also been optimized in three spin states: $Fe^{2+,LS}$−(HO−O)$^-$−Cu^+, $Fe^{2+,IS}$−(HO−O)$^-$−Cu^+, and $Fe^{2+,HS}$−(HO−O)$^-$−Cu^+. The main calculated properties of the optimized structures are given in Table 5. The central portions of the DNC of the optimized $Fe^{2+,LS}$−(HO−O)$^-$−Cu^+ and $Fe^{2+,IS}$−(HO−O)$^-$−Cu^+ geometries

dx.doi.org/10.1021/ic401858s | Inorg. Chem. 2013, 52, 14072−14088

Table 5. Calculated Properties of the Fe^{2+}−(HO−O)$^-$−Cu^+ (Figure 5) DNC Models in Different Spin States Using OLYP Potential[a]

	geometry										RMSD			net spin			
state	O1−O2	Fe−O1	Fe−N (H384)	Cu−O2	Cu−N (H233)	Cu−N (H282)	Cu−N (H283)	Fe···Cu	O···O (Y237)	Fe−O1−O2	Fe−O1−O2−Cu	5-atom	8-atom	all	E	Fe	Cu	O1	O2
$Fe^{2+,LS}$−(HO−O)$^-$−Cu^+	1.55	2.05	2.06	1.90	2.93	2.00	2.32	4.48	3.41	122	−111	0.57	0.52	0.43	−96.72	0.00	0.00	0.00	0.00
$Fe^{2+,IS}$−(HO−O)$^-$−Cu^+	1.46	2.92	2.26	1.97	2.21	2.10	2.14	5.25	3.35	137	−124	0.36	0.39	0.33	−90.90	2.04	0.28	0.07	0.18
$Fe^{2+,HS}$−(HO−O)$^-$−Cu^+	1.48	2.99	2.17	1.98	2.28	2.10	2.19	5.35	3.38	134	−123	0.35	0.40	0.36	−90.62	3.74	0.17	0.04	0.09
av-xyz[b]	1.49	2.65	2.16	1.95	2.46	2.05	2.20	5.02	3.38	128	−118	0.28	0.34	0.36					
exptl X-ray 3S8G	1.52	2.39	2.22	2.25	1.95	2.03	1.98	4.92	2.66	140	−147								

[a]The properties include geometry (Å, deg), RMSD (Å), electronic energy (E, −28000 kcal mol^{-1}), and the Mulliken net spin polarizations for Fe^{2+}, Cu^+, O1, and O2 atoms. See footnotes b−e of Table 1. [b]This structure is obtained by averaging the Cartesian coordinates of all the optimized Fe^{2+}−(HO−O)$^-$−Cu^+ DNC clusters.

are shown in Figures 11 and 12, respectively. The overall geometry of the $Fe^{2+,HS}$−(HO−O)$^-$−Cu^+ state is very similar to that of the $Fe^{2+,IS}$−(HO−O)$^-$−Cu^+ state.

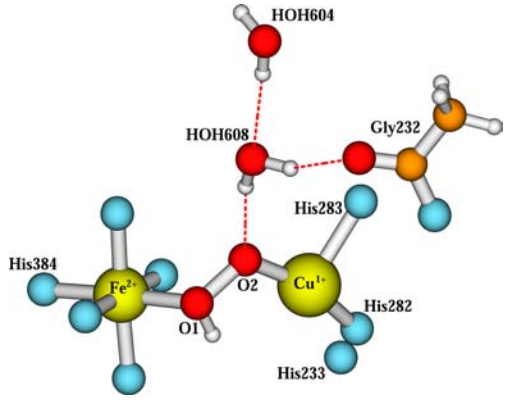

Figure 11. Central portion of the DNC of the optimized $Fe^{2+,LS}$−(HO−O)$^-$−Cu^+ cluster, where a proton binds with O1.

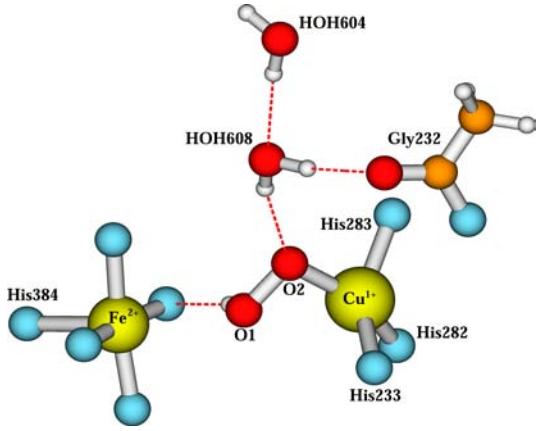

Figure 12. Central portion of the DNC of the optimized $Fe^{2+,IS}$−(HO−O)$^-$−Cu^+ cluster, where a proton binds with O1. The optimized $Fe^{2+,HS}$−(HO−O)$^-$−Cu^+ structure is very similar to this.

Similar to the case for the Fe^{2+}−(O−OH)$^-$−Cu^+ clusters, the O1−O2 bond lengths (1.46−1.55 Å) of the optimized Fe^{2+}−(HO−O)$^-$−Cu^+ structures agree with experiment (1.52 Å) very well. However, the optimized $Fe^{2+,LS}$−(HO−O)$^-$−Cu^+ state has a very large RMSD(5-atom) value (0.57 Å), mainly because of its short Fe−O1, Cu−O2, and Fe···Cu distances. This structure also yields a very large RMSD(8-atom) value (0.52 Å), resulting from its long Cu−N(His233) and Cu−N(His283) distances.

In contrast, the calculated RMSD(5-atom) values for the optimized $Fe^{2+,IS}$−(HO−O)$^-$−Cu^+ and $Fe^{2+,HS}$−(HO−O)$^-$−Cu^+ structures are only 0.36 and 0.35 Å, respectively, which are so far the smallest among all the calculated RMSD(5-atom) values. Although the Fe−O1 distances (2.92−2.99 Å) in these two optimized clusters are much longer than the experimental value (2.39 Å), the overall features of the two structures are close to the experiment: i.e., the O1−O2 bond length is close to 1.52 Å, Cu−O2 is shorter than Fe−O1, and Fe−O1 is longer than Fe−N(His384). None of the optimized structures in all of our calculations reproduces the exact positions and the orientations (∠Fe−O1−O2 and ∠Fe−O1−O2−Cu) of the O1 and O2 atoms in 3S8G.pdb. However, the calculated ∠Fe−O1−O2

dx.doi.org/10.1021/ic401858s | Inorg. Chem. 2013, 52, 14072−14088

and torsion ∠Fe−O1−O2−Cu values in the optimized $Fe^{2+,IS}$−(HO−O)$^-$−Cu^+ and $Fe^{2+,HS}$−(HO−O)$^-$−Cu^+ structures are close to the experiment.

Further, we also calculated the average of the Cartesian coordinates (av-*xyz* in Table 5) of these three optimized Fe^{2+}−(HO−O)$^-$−Cu^+ structures. Surprisingly, the calculated RMSD(5-atom) value for this av-*xyz* is only 0.28 Å, which is 0.07−0.31 Å smaller than all other calculated RMSD(5-atom) values presented in Tables 1−5.

The electronic energy of the $Fe^{2+,LS}$−(HO−O)$^-$−Cu^+ state is ∼6 kcal mol^{-1} lower than the $Fe^{2+,IS}$−(HO−O)$^-$−Cu^+ and $Fe^{2+,HS}$−(HO−O)$^-$−Cu^+ states. As discussed earlier, considering the DFT calculation errors, the zero-point energy (ZPE) and entropy terms (not calculated here, but both vibrational entropy and vibrational ZPE terms most likely favor the $Fe^{2+,HS}$ state and favor $Fe^{2+,IS}$ over the $Fe^{2+,LS}$ state), and if the Fe site of the oxidized as-isolated protein was originally in the HS state, upon reduction it may still stay in HS (or first change to IS before going to LS). It is feasible that the $Fe^{2+,LS}$−(HO−O)$^-$−Cu^+, $Fe^{2+,IS}$−(HO−O)$^-$−Cu^+, and $Fe^{2+,HS}$−(HO−O)$^-$−Cu^+ states may coexist in the radiation-reduced crystal at low temperature. In this case, the experimentally observed dioxygen O1−O2 in the DNC of the 3S8G crystal structure is HO_2^-, and the DNC structure in 3S8G reflects the superposition of three DNC conformations: $Fe^{2+,LS}$−(HO−O)$^-$−Cu^+, $Fe^{2+,IS}$−(HO−O)$^-$−Cu^+, and $Fe^{2+,HS}$−(HO−O)$^-$−Cu^+.

Although it was indicated in ref 38 that the electron density distribution between Fe_{a3} and Cu_B observed in the fully oxidized bovine heart *C*cO X-ray crystal structure (2.3 Å resolution) in ref 36 should be considered as a preliminary result, it is worth noting that the electron density between the two metals in the 2.3 Å resolution structure is also consistent with the conformation Fe_{a3}···(HO−O)−Cu_B, where a hydroperoxo ligand binds with Cu_B (see footnote 9 of ref 36). It is not certain whether this 2.3 Å resolution structure was radiolytically reduced or not. If it were, then its DNC would be in the Fe^{2+}−(HO−O)$^-$−Cu^+ state, which is consistent with our calculations in this section.

Note that the electronic energy of the $Fe^{2+,LS}$−(O−OH)$^-$−Cu^+ state (Figure 9 and Table 4) is 5.6 kcal mol^{-1} lower than the $Fe^{2+,LS}$−(HO−O)$^-$−Cu^+ state, and even the $Fe^{2+,IS}$−(O−OH)$^-$−Cu^+ and $Fe^{2+,HS}$−(O−OH)$^-$−Cu^+ states are lower in energy than the $Fe^{2+,LS}$−(HO−O)$^-$−Cu^+ state. Consequently, we propose that the DNC is structurally trapped in the Fe^{2+}−(HO−O)$^-$−Cu^+ state during the X-ray irradiation at low temperature; however, one cannot exclude the possibility that some Fe^{2+}−(O−OH)$^-$−Cu^+ structures coexist with the Fe^{2+}−(HO−O)$^-$−Cu^+ state. We will further study the superposition of the Fe^{2+}−(O−OH)$^-$−Cu^+ and Fe^{2+}−(HO−O)$^-$−Cu^+ states (with deprotonated Tyr237$^-$ side chain) in section 4.4.5.

So far, we have treated the Tyr237 side chain as neutral in all our calculations (Tables 1−5). We notice that the O···O distance between the Tyr237 side chain and the geranyl side chain of a_3-heme (see Figure 3) is only 2.66 Å in the X-ray crystal structure. However, this H-bonding distance in all our geometry optimized clusters is well over 3.0 Å (see Tables 4 and 5). Therefore, the Tyr237 in the radiation-reduced crystal is probably in the deprotonated Tyr237$^-$ anion form.[65] This result motivated us to look more closely at the geometric effects of this charged versus neutral O···O hydrogen bond. We have geometry optimized the Fe^{2+}−(O−OH)$^-$−Cu^+ and Fe^{2+}−(HO−O)$^-$−Cu^+ clusters with the Tyr237$^-$ side chain, labeled as Fe^{2+}−(O−OH)$^-$−Cu^+(Y237$^-$) and Fe^{2+}−(HO−O)$^-$−Cu^+(Y237$^-$), in different spin states (LS, IS, and HS). The calculated results of these clusters with Tyr237$^-$ side chain are given below.

4.4.3. Fe^{2+}−(O−OH)$^-$−Cu^+(Y237$^-$) DNC Calculations. The calculated properties of the geometry optimized $Fe^{2+,LS}$−(O−OH)$^-$−Cu^+(Y237$^-$), $Fe^{2+,IS}$−(O−OH)$^-$−Cu^+(Y237$^-$), and $Fe^{2+,HS}$−(O−OH)$^-$−Cu^+(Y237$^-$) clusters are given in Table 6. The H-bonding O···O distance between the Tyr237-O$^-$ and the geranyl −OH of the a_3-heme decreases by 0.3−0.4 Å relative to the corresponding neutral Tyr237 structures (Table 4), which indicates the Tyr237 side chain is likely deprotonated in the 3S8G X-ray crystal structure. However, other features of these three DNC models are still not consistent with experiment. Their Cu−O2 distances and the Fe−N(His384) distance in $Fe^{2+,HS}$−(O−OH)$^-$−Cu^+(Y237$^-$) are even longer than the corresponding values in Table 4. In general, the RMSD values of these three Fe^{2+}−(O−OH)$^-$−Cu^+(Y237$^-$) structures and their av-*xyz* structures are equal to or worse than the corresponding RMSD's of the Fe^{2+}−(O−OH)$^-$−Cu^+ cluster given in Table 4. Again, the individual or the supposition of these three Fe^{2+}−(O−OH)$^-$−Cu^+(Y237$^-$) clusters is not consistent with the DNC structure observed in 3S8G.pdb.

With the energies of the Fe^{2+}−(O−OH)$^-$−Cu^+ (protonated Tyr237) and Fe^{2+}−(O−OH)$^-$−Cu^+(Y237$^-$) (deprotonated Tyr237) states, one can estimate the proton affinity (PA) and pK_a values for the Tyr237 side chain. However, bearing in mind that the experimental system being analyzed is far from an equilibrium state (low temperature, inhibiting proton mobility with aquated electrons from X-ray irradiation), the following analyses for PA and pK_a values are for the equilibrium state at room temperature:[11,56]

$$\begin{aligned}\mathrm{PA} = {} & E[\mathrm{Fe}^{2+}-(\mathrm{HO_2})^-\mathrm{-Cu}^+(\mathrm{Y237}^-)] \\ & - E[\mathrm{Fe}^{2+}-(\mathrm{HO_2})^-\mathrm{-Cu}^+] + E(\mathrm{H}^+) - T\Delta S_{\mathrm{gas}}(\mathrm{H}^+) \\ & + \Delta\mathrm{ZPE} + (5/2)RT \end{aligned} \quad (1)$$

$$\begin{aligned}1.37\mathrm{p}K_a = {} & E[\mathrm{Fe}^{2+}-(\mathrm{HO_2})^-\mathrm{-Cu}^+(\mathrm{Y237}^-)] \\ & - E[\mathrm{Fe}^{2+}-(\mathrm{HO_2})^-\mathrm{-Cu}^+] + E(\mathrm{H}^+) \\ & + \Delta G_{\mathrm{sol}}(\mathrm{H}^+,1\ \mathrm{atm}) - T\Delta S_{\mathrm{gas}}(\mathrm{H}^+) + \Delta\mathrm{ZPE} \\ & + (5/2)RT \end{aligned} \quad (2)$$

where $\Delta G_{sol}(H^+,1\ atm)$ is the solvation free energy of a proton at 1 atm pressure. We will use −263.98 kcal mol^{-1} for this term, since so far it is the best measured value.[66−68] $E(H^+)$ = 291.44 kcal mol^{-1} is the calculated energy of a proton (in the gas phase with OLYP potential) with respect to a spin-restricted hydrogen atom. The translational entropy contribution to the gas-phase free energy of a proton is taken as $-T\Delta S_{gas}(H^+)$ = −7.76 kcal mol^{-1} at 298 K and 1 atm pressure.[69] $(5/2)RT$ includes the proton translational energy $(3/2)RT$ and $PV = RT$.[69] The zero point energy difference term ΔZPE was calculated as −8.03 kcal mol^{-1} for a Tyr side chain in our previous study using OPBE potential.[56]

Taking the energy terms $E[Fe^{2+}-(HO_2)^-\mathrm{-Cu}^+(Y237^-)]$ and $E[Fe^{2+}-(HO_2)^-\mathrm{-Cu}^+]$ from Tables 6 and 4, we obtain PA = 279.7, 279.9, and 275.97 kcal mol^{-1}, and pK_a = 11.5, 11.6, and 8.8, for the Tyr237 side chain in the $Fe^{2+,LS}$−(O−OH)$^-$−Cu^+, $Fe^{2+,IS}$−(O−OH)$^-$−Cu^+, and $Fe^{2+,HS}$−(O−OH)$^-$−Cu^+ states, respectively. Therefore, in the equilibrium state, Tyr237 is likely to be in the neutral protonated state.

dx.doi.org/10.1021/ic401858s | *Inorg. Chem.* 2013, 52, 14072−14088

Table 6. Calculated Properties of the Fe^{2+}−(O−OH)$^-$−Cu^+(Y237$^-$) DNC Models in Different Spin States Using OLYP Potential[a]

state	geometry										RMSD			net spin			
	O1−O2	Fe−O1	Fe−N (H384)	Cu−O2	Cu−N (H233)	Cu−N (H282)	Cu−N (H283)	Fe···Cu	O···O (Y237$^-$)	Fe−O1−O2	Fe−O1−O2−Cu	5-atom	8-atom	all	E	Fe	Cu	O1	O2
$Fe^{2+,LS}$−(O−OH)$^-$−Cu^+(Y237$^-$)	1.49	1.86	2.18	3.04	2.02	2.09	2.06	5.34	2.82	115	−130	0.59	0.56	0.38	−99.77	0.00	0.00	0.00	0.00
$Fe^{2+,IS}$−(O−OH)$^-$−Cu^+(Y237$^-$)	1.47	1.98	2.70	3.38	2.01	2.11	2.07	5.14	3.04	119	−141	0.54	0.57	0.41	−95.69	2.15	0.00	0.34	0.05
$Fe^{2+,HS}$−(O−OH)$^-$−Cu^+(Y237$^-$)	1.47	1.96	2.74	3.45	2.01	2.10	2.08	5.08	2.90	127	−146	0.56	0.60	0.42	−98.19	3.82	0.00	0.34	0.04
av-*xyz*[b]	1.42	1.93	2.54	3.27	2.01	2.10	2.07	5.19	2.92	120	−136	0.51	0.54	0.39					
exptl X-ray 3S8G	1.52	2.39	2.22	2.25	1.95	2.03	1.98	4.92	2.66	140	−147								

[a]The properties include geometry (Å, deg), RMSD (Å), electronic energy (E, −28000 kcal mol^{-1}), and the Mulliken net spin polarizations for Fe^{2+}, Cu^+, O1, and O2 atoms. See footnotes b−e of Table 1. [b]This structure is obtained by averaging the Cartesian coordinates of all the optimized Fe^{2+}−(O−OH)$^-$−Cu^+(Y237$^-$) DNC clusters.

4.4.4. Fe^{2+}−(HO−O)$^-$−Cu^+(Y237$^-$) DNC Calculations. The calculated properties of the geometry optimized $Fe^{2+,LS}$−(HO−O)$^-$−Cu^+(Y237$^-$), $Fe^{2+,IS}$−(HO−O)$^-$−Cu^+(Y237$^-$), and $Fe^{2+,HS}$−(HO−O)$^-$−Cu^+(Y237$^-$) clusters are given in Table 7.

From eqs 1 and 2, using the energies of the Fe^{2+}−(HO−O)$^-$−Cu^+(Y237$^-$) and Fe^{2+}−(HO−O)$^-$−Cu^+ clusters from Tables 7 and 5, we then obtain PA =283.1, 279.9, and 282.6 kcal mol^{-1} and pK_a = 13.9, 11.6, and 13.6, respectively, for the Tyr237 side chain of the three $Fe^{2+,LS}$−(HO−O)$^-$−Cu^+, $Fe^{2+,IS}$−(HO−O)$^-$−Cu^+, and $Fe^{2+,HS}$−(HO−O)$^-$−Cu^+ clusters in the equilibrium state at room temperature (T = 298 K). These PA and pK_a values also show that the Tyr237 side chain of the Fe^{2+}−(HO−O)$^-$−Cu^+ clusters should mainly be in the neutral form in the equilibrium state.

However, in the above three states, changing Tyr237 to Tyr237$^-$, the H-bonding O···O distance between the Tyr237 −O$^-$ and the geranyl −OH of the a_3-heme decreases from ∼3.4 Å to ∼2.8 Å, which is much closer to the experimental value of 2.66 Å. The calculated RMSD(all) values of the $Fe^{2+,IS}$−(HO−O)$^-$−Cu^+(Y237$^-$) and the $Fe^{2+,IS}$−(HO−O)$^-$−Cu^+ states are the same (0.33 Å). However, the RMSD(all) values of the $Fe^{2+,LS}$−(HO−O)$^-$−Cu^+(Y237$^-$) and $Fe^{2+,HS}$−(HO−O)$^-$−Cu^+(Y237$^-$) states are smaller by 0.04−0.05 Å than those of the corresponding $Fe^{2+,LS}$−(HO−O)$^-$−Cu^+ and $Fe^{2+,HS}$−(HO−O)$^-$−Cu^+ states. Therefore, if the Fe^{2+}−(HO−O)$^-$−Cu^+ structure represents the DNC of the 3S8G X-ray crystal structure, it is highly likely that Tyr237 is trapped in the Tyr237$^-$ deprotonated form.

Changing Tyr237 from the neutral form to the anionic form does not have major effects on the central Fe−O1−O2−Cu conformation for the $Fe^{2+,IS}$−(HO−O)$^-$−Cu^+ and the $Fe^{2+,HS}$−(HO−O)$^-$−Cu^+ states; however, it does affect the $Fe^{2+,LS}$−(HO−O)$^-$−Cu^+ state. From $Fe^{2+,LS}$−(HO−O)$^-$−Cu^+ to $Fe^{2+,LS}$−(HO−O)$^-$−Cu^+(Y237$^-$), the Cu−N(His233) and Cu−N(His283) distances are shortened by 0.39 and 0.07 Å, respectively, and the Fe···Cu distance is increased by 0.15 Å. As a result, the calculated RMSD(5-atom) and RMSD(8-atom) values are decreased by 0.08 and 0.07 Å, respectively.

The electronic energy difference between the $Fe^{2+,LS}$−(HO−O)$^-$−Cu^+(Y237$^-$) and the $Fe^{2+,HS}$−(HO−O)$^-$−Cu^+(Y237$^-$) states is 5.7 kcal mol^{-1}. The energy difference between the $Fe^{2+,LS}$−(HO−O)$^-$−Cu^+(Y237$^-$) and the $Fe^{2+,IS}$−(HO−O)$^-$−Cu^+(Y237$^-$) states is only 2.6 kcal mol^{-1}. It is quite possible that these three Fe^{2+}−(HO−O)$^-$−Cu^+(Y237$^-$) states coexist after the X-ray irradiation, considering also the expected shift in relative free energies from ZPE and vibrational entropy.

We have calculated the average of the Cartesian coordinates of these three Fe^{2+}−(HO−O)$^-$−Cu^+(Y237$^-$) optimized geometries (see av-*xyz* in Table 7). Figure 13 shows the overlap of this av-*xyz* structure (in red, without water molecules) and the 3S8G X-ray crystal structure (in blue). The calculated RMSD(5-atom), RMSD(8-atom), and RMSD(all) values between this av-*xyz* and the X-ray crystal structure are 0.29, 0.34, and 0.33 Å, respectively.

In addition, we found that the potential energy surface along the Fe···Cu distance in the $Fe^{2+,LS}$−(HO−O)$^-$−Cu^+(Y237$^-$) state is very flat. We obtained two additional local minima of the $Fe^{2+,LS}$−(HO−O)$^-$−Cu^+(Y237$^-$) state with much longer Fe···Cu distances but with very similar energies. The properties of these two structures, named as $Fe^{2+,LS}$−(HO−O)$^-$−Cu^+(Y237$^-$)$^{(2)}$ and $Fe^{2+,LS}$−(HO−O)$^-$−Cu^+(Y237$^-$)$^{(3)}$, are

Table 7. Calculated Properties of the Fe^{2+}–(HO–O)$^-$–Cu^+($Y237^-$) DNC Models in Different Spin States Using OLYP Potential[a]

	geometry										RMSD				net spin			
state	O1–O2	Fe–O1	Fe–N (H384)	Cu–O2	Cu–N (H233)	Cu–N (H282)	Cu–N (H283)	Fe···Cu	O···O ($Y237^-$)	Fe–O1–O2	Fe–O1–O2–Cu	5-atom	8-atom	all	E	Fe	Cu	O1	O2
$Fe^{2+,LS}$–(HO–O)$^-$–Cu^+($Y237^-$)	1.54	2.06	2.07	1.94	2.54	2.05	2.25	4.63	2.81	125	−116	0.49	0.45	0.38	−90.80	0.00	0.00	0.00	0.00
$Fe^{2+,IS}$–(HO–O)$^-$–Cu^+($Y237^-$)	1.47	2.90	2.26	1.98	2.17	2.10	2.17	5.25	2.88	139	−124	0.38	0.41	0.33	−88.16	2.08	0.28	0.07	0.18
$Fe^{2+,HS}$–(HO–O)$^-$–Cu^+($Y237^-$)	1.48	2.98	2.17	1.99	2.20	2.10	2.19	5.33	2.82	134	−125	0.34	0.38	0.32	−85.11	3.72	0.24	0.05	0.13
av-*xyz*[b]	1.49	2.64	2.16	1.97	2.29	2.08	2.20	5.07	2.83	134	−120	0.29	0.34	0.33					
exptl X-ray 3S8G	1.52	2.39	2.22	2.25	1.95	2.03	1.98	4.92	2.66	140	−147								

[a]The properties include geometry (Å, deg), RMSD (Å), electronic energy (E, −28000 kcal mol^{-1}), and the Mulliken net spin polarizations for Fe^{2+}, Cu^+, O1, and O2 atoms. See footnotes b–e of Table 1. [b]This structure is obtained by averaging the Cartesian coordinates of all the optimized Fe^{2+}–(HO–O)$^-$–Cu^+($Y237^-$) DNC clusters.

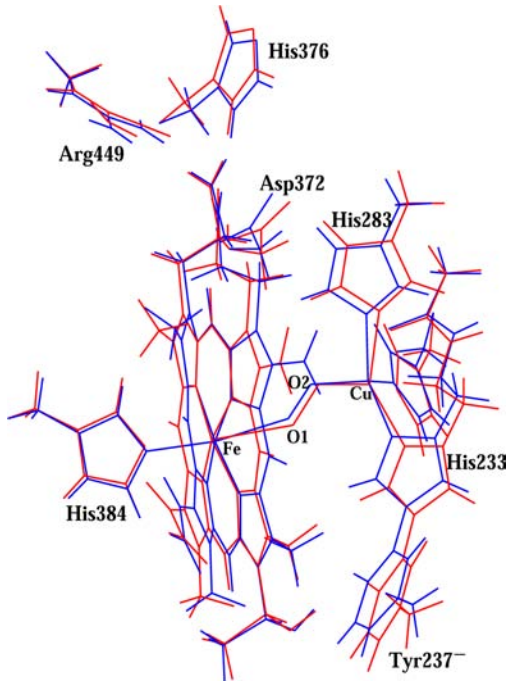

Figure 13. Overlap of the DNC of the 3S8G X-ray crystal structure (in blue, without water molecules) and the av-*xyz* (in red) structure of the three $Fe^{2+,LS}$–(HO–O)$^-$–Cu^+($Y237^-$), $Fe^{2+,IS}$–(HO–O)$^-$–Cu^+($Y237^-$) and $Fe^{2+,HS}$–(HO–O)$^-$–Cu^+($Y237^-$) optimized clusters.

given in Table 8, along with the lowest energy state $Fe^{2+,LS}$–(HO–O)$^-$–Cu^+($Y237^-$)$^{(1)}$ (which is the $Fe^{2+,LS}$–(HO–O)$^-$–Cu^+($Y237^-$) state in Table 7).

The Fe···Cu distances in $Fe^{2+,LS}$–(HO–O)$^-$–Cu^+($Y237^-$)$^{(2)}$ and $Fe^{2+,LS}$–(HO–O)$^-$–Cu^+($Y237^-$)$^{(3)}$ (Table 8) are 4.91 and 5.10 Å, respectively, which are much closer to the experimental value (4.92 Å) and 0.28 and 0.37 Å longer than the Fe···Cu distance of the lowest-energy $Fe^{2+,LS}$–(HO–O)$^-$–Cu^+($Y237^-$)$^{(1)}$ structure (4.63 Å). However, these two local-minimum structures are only 1.2 and 2.6 kcal mol^{-1} higher than the lowest-energy cluster. Bear in mind that these energies are only electronic energies. If one considers the ZPE and entropy terms, these energy differences may be even smaller.

The overall structural features of $Fe^{2+,LS}$–(HO–O)$^-$–Cu^+($Y237^-$)$^{(3)}$ are very similar to the 3S8G crystal structure, especially for the O1–O2, Fe–O1, and Fe···Cu distances and the O1–O2 orientation. The positions of the central eight atoms Fe, N(His384), O1, O2, Cu, N(His233), N(His282), and N(His283) in 3S8G.pdb[42] and in $Fe^{2+,LS}$–(HO–O)$^-$–Cu^+($Y237^-$)$^{(3)}$ are compared in Figure 14. The calculated RMSD-(5-atom) value of the $Fe^{2+,LS}$–(HO–O)$^-$–Cu^+($Y237^-$)$^{(3)}$ structure is 0.32 Å, which is the smallest among all RMSD(5-atom) values for the individual model clusters.

Therefore, if the $Fe^{2+,IS}$–(HO–O)$^-$–Cu^+($Y237^-$) and the $Fe^{2+,HS}$–(HO–O)$^-$–Cu^+($Y237^-$) states do not coexist with the $Fe^{2+,LS}$–(HO–O)$^-$–Cu^+($Y237^-$) state but rather change to the $Fe^{2+,LS}$–(HO–O)$^-$–Cu^+($Y237^-$) state alone, the experimentally observed structure is possibly the $Fe^{2+,LS}$–(HO–O)$^-$–Cu^+($Y237^-$) state, very close to the $Fe^{2+,LS}$–(HO–O)$^-$–Cu^+($Y237^-$)$^{(3)}$ structure. In the as-isolated oxidized state, with a H_2O···OH^- pair (or a related form) binding between the Fe^{3+} and Cu^{2+} sites, the Fe^{3+}···Cu^{2+} distance should be much longer than 4.6 Å (the Fe···Cu distance in $Fe^{3+,LS}$–O_2^{2-}–Cu^{2+}(F), see Table 1). Upon the metal site reduction during X-ray

Table 8. Calculated Properties of the Local Minima of the $Fe^{2+,LS}$–(HO–O)$^-$–Cu^+(Y237$^-$) State Using OLYP Potential[a,b]

state	geometry										RMSD		net spin				
	O1–O2	Fe–O1	Fe–N (H384)	Cu–O2	Cu–N (H233)	Cu–N (H282)	Cu–N (H283)	Fe···Cu	O···O (Y237$^-$)	Fe–O1–O2–Cu	5-atom	8-atom	all	E	Fe	Cu	O1	O2
$Fe^{2+,LS}$–(HO–O)$^-$–Cu^+(Y237$^-$)$^{(1)}$	1.54	2.06	2.07	1.94	2.54	2.05	2.25	4.63	2.81	125	−116	0.49	0.45	0.38	−90.80	0.00	0.00	0.00	0.00
$Fe^{2+,LS}$–(HO–O)$^-$–Cu^+(Y237$^-$)$^{(2)}$	1.53	2.19	2.07	2.03	2.28	2.18	2.26	4.91	2.84	129	−137	0.39	0.43	0.40	−89.62	0.00	0.00	0.00	0.00
$Fe^{2+,LS}$–(HO–O)$^-$–Cu^+(Y237$^-$)$^{(3)}$	1.51	2.40	2.04	2.05	2.23	2.19	2.23	5.10	2.88	132	−140	0.32	0.40	0.39	−88.22	0.00	0.00	0.00	0.00
exptl X-ray 3S8G	1.52	2.39	2.22	2.25	1.95	2.03	1.98	4.92	2.66	140	−147								

[a]The properties include geometry (Å, deg), RMSD (Å), electronic energy (E, −28000 kcal mol^{-1}), and the Mulliken net spin polarizations for Fe^{2+}, Cu^+, O1, and O2 atoms. The lowest-energy structure $Fe^{2+,LS}$–(HO–O)$^-$–Cu^+(Y237$^-$)$^{(1)}$ was also given in Table 7 as $Fe^{2+,LS}$–(HO–O)$^-$–Cu^+(Y237$^-$). [b]Also see footnotes b–e of Table 1.

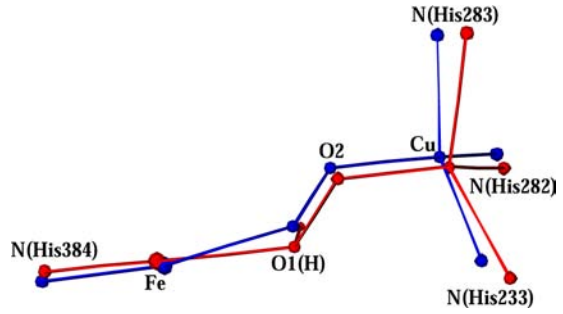

Figure 14. Comparison of the positions of Fe, N(His384), O1(H), O2, Cu, N(His233), N(His282), and N(His283) in the DNC's of 3S8G.pdb (blue) and $Fe^{2+,LS}$–(HO–O)$^-$–Cu^+(Y237$^-$)$^{(3)}$ (red).

irradiation, although the lowest electronic energy $Fe^{2+,LS}$–(HO–O)$^-$–Cu^+(Y237$^-$) state favors a short 4.63 Å Fe···Cu distance (Table 7), since the shrinking of the Fe···Cu distance costs reorganization energy, the radiation-reduced protein may be trapped near the local minimum $Fe^{2+,LS}$–(HO–O)$^-$–Cu^+(Y237$^-$)$^{(3)}$ structure, which is calculated to be only about 2.6 kcal mol^{-1} higher in energy than the lowest-energy structure.

4.4.5. Mixture of the Fe^{2+}–(HO–O)$^-$–Cu^+(Y237$^-$) and Fe^{2+}–(O–OH)$^-$–Cu^+(Y237$^-$) States. Although any of the Fe^{2+}–(O–OH)$^-$–Cu^+ and the Fe^{2+}–(O–OH)$^-$–Cu^+(Y237$^-$) clusters alone is unlikely to represent the DNC of the 3S8G crystal structure, the Fe^{2+}–(O–OH)$^-$–Cu^+/Fe^{2+}–(O–OH)$^-$–Cu^+(Y237$^-$) structures (Tables 4 and 6) are typically lower in energy than the comparable Fe^{2+}–(HO–O)$^-$–Cu^+/Fe^{2+}–(HO–O)$^-$–Cu^+(Y237$^-$) structures (Tables 5 and 7). The electronic energy difference between $Fe^{2+,LS}$–(O–OH)$^-$–Cu^+(Y237$^-$) and $Fe^{2+,LS}$–(HO–O)$^-$–Cu^+(Y237$^-$) is 9 kcal mol^{-1}. Here we briefly examine the feasibility of trapping the higher energy Fe^{2+}–(HO–O)$^-$–Cu^+(Y237$^-$) state (vs Fe^{2+}–(O–OH)$^-$–Cu^+(Y237$^-$)) by analyzing the expected free energy barrier ($\Delta G^{\ddagger}$). We use standard transition state theory to calculate an approximate minimum free energy barrier under experimental conditions. From ref 42, the X-ray experimental temperature is T = 100 K, and the radiation-damaged crystals are translated after 20 s (20 frames at 1 s exposure). Therefore, for a rough estimate of the minimum $\Delta G^{\ddagger}$ value, let the half-life $t_{1/2}$ = 20 s for conversion of the trapped state Fe^{2+}–(HO–O)$^-$–Cu^+(Y237$^-$) → Fe^{2+}–(O–OH)$^-$–Cu^+(Y237$^-$). Then standard transition state theory predicts $\Delta G^{\ddagger}$ = 6.3 kcal mol^{-1} (at 100 K). The calculation shows, if the barrier is increased by only 0.5 kcal mol^{-1} (to 6.8 kcal mol^{-1}), the conversion rate constant will be drastically lowered by a factor of 10; therefore, the Fe^{2+}–(O–OH)$^-$–Cu^+(Y237$^-$) state would be barely observable, at best.

The corresponding Fe^{2+}–(HO–O)$^-$–Cu^+(Y237$^-$) → Fe^{2+}–(O–OH)$^-$–Cu^+(Y237$^-$) structural transformation involves Cu–O bond breaking, Fe–O bond making, a proton transfer, shifts in H-bonding patterns, and structural rearrangement of HO_2^- and the whole cluster (compare Figures 9 and 10 to Figures 11 and 12). All of these are expected to require a barrier much higher than the estimated $\Delta G^{\ddagger}$ = 6.3–6.8 kcal mol^{-1}. The low temperature of the experiment (T = 100 K) is critically important, and much higher temperatures are expected to give much higher conversion rates, so that the Fe^{2+}–(O–OH)$^-$–Cu^+(Y237$^-$) state could become the dominant species. This result will depend on the actual conversion barrier.

Although the conversion Fe^{2+}–(HO–O)$^-$–Cu^+(Y237$^-$) → Fe^{2+}–(O–OH)$^-$–Cu^+(Y237$^-$) may not be feasible at low

Table 9. Comparison of the av-*xyz* Structures of the Fe^{2+}−(HO−O)$^-$−Cu^+(Y237$^-$) and Fe^{2+}−(O−OH)$^-$−Cu^+(Y237$^-$) States with the 3S8G X-ray Crystal Structure[a]

	geometry											RMSD		
av-*xyz*	O1−O2	Fe−O1	Fe−N (H384)	Cu−O2	Cu−N (H233)	Cu−N (H282)	Cu−N (H283)	Fe−Cu	O···O (Y237$^-$)	Fe−O1−O2	Fe−O1−O2−Cu	5-atom	8-atom	all
(1)[b]	1.49	2.44	2.17	2.22	2.21	2.07	2.15	5.13	2.83	130	−124	0.31	0.35	0.34
(2)[c]	1.43	2.28	2.35	2.61	2.13	2.08	2.12	5.12	2.88	128	−130	0.32	0.39	0.35
from Table6 [d]	1.42	1.93	2.54	3.27	2.01	2.10	2.07	5.19	2.92	120	−136	0.51	0.54	0.39
from Table7 [e]	1.49	2.64	2.16	1.97	2.29	2.08	2.20	5.07	2.83	134	−120	0.29	0.34	0.33
exptl X-ray 3S8G	1.52	2.39	2.22	2.25	1.95	2.03	1.98	4.92	2.66	140	−147			

[a]See footnote b of Table 1. [b]The average of the Cartesian coordinates of the following four structures: $Fe^{2+,LS}$−(O−OH)$^-$−Cu^+(Y237$^-$), $Fe^{2+,LS}$−(HO−O)$^-$−Cu^+(Y237$^-$), $Fe^{2+,IS}$−(HO−O)$^-$−Cu^+(Y237$^-$), and $Fe^{2+,HS}$−(HO−O)$^-$−Cu^+(Y237$^-$). [c]The average of the Cartesian coordinates of all six structures given in Tables 6 and 7: $Fe^{2+,LS}$−(O−OH)$^-$−Cu^+(Y237$^-$), $Fe^{2+,IS}$−(O−OH)$^-$−Cu^+(Y237$^-$), $Fe^{2+,HS}$−(O−OH)$^-$−Cu^+(Y237$^-$), $Fe^{2+,LS}$−(HO−O)$^-$−Cu^+(Y237$^-$), $Fe^{2+,IS}$−(HO−O)$^-$−Cu^+(Y237$^-$), and $Fe^{2+,HS}$−(HO−O)$^-$−Cu^+(Y237$^-$). [d]For comparison, the av-*xyz* values of the three Fe^{2+}−(O−OH)$^-$−Cu^+(Y237$^-$) states in Table 6 are also shown here. [e]For comparison, the av-*xyz* values of the three Fe^{2+}−(HO−O)$^-$−Cu^+(Y237$^-$) states in Table 7 are also shown here.

temperature, one cannot exclude the possibility that the Fe^{2+}−(O−OH)$^-$−Cu^+(Y237$^-$) state clusters may coexist with the Fe^{2+}−(HO−O)$^-$−Cu^+(Y237$^-$) state. To see if the superposition of the DNC clusters of these two states agrees with the DNC of the X-ray crystal structure, we have calculated the average of the Cartesian coordinates in two cases: (1) the average of the four structures $Fe^{2+,LS}$−(O−OH)$^-$−Cu^+(Y237$^-$), $Fe^{2+,LS}$−(HO−O)$^-$−Cu^+(Y237$^-$), $Fe^{2+,IS}$−(HO−O)$^-$−Cu^+(Y237$^-$), and $Fe^{2+,HS}$−(HO−O)$^-$−Cu^+(Y237$^-$); and (2) the average of all six structures given in Tables 6 and 7 $Fe^{2+,LS}$−(O−OH)$^-$−Cu^+(Y237$^-$), $Fe^{2+,IS}$−(O−OH)$^-$−Cu^+(Y237$^-$), $Fe^{2+,HS}$−(O−OH)$^-$−Cu^+(Y237$^-$), $Fe^{2+,LS}$−(HO−O)$^-$−Cu^+(Y237$^-$), $Fe^{2+,IS}$−(HO−O)$^-$−Cu^+(Y237$^-$), and $Fe^{2+,HS}$−(HO−O)$^-$−Cu^+(Y237$^-$). The geometrical properties of these two averaged *xyz* structures (av-*xyz*(1) and av-*xyz*(2)) are given in Table 9 and are compared with the experimental values and with the av-*xyz* values from Tables 6 and 7.

In case 1, adding $Fe^{2+,LS}$−(O−OH)$^-$−Cu^+(Y237$^-$) to the mixture of $Fe^{2+,LS}$−(HO−O)$^-$−Cu^+(Y237$^-$), $Fe^{2+,IS}$−(HO−O)$^-$−Cu^+(Y237$^-$), and $Fe^{2+,HS}$−(HO−O)$^-$−Cu^+(Y237$^-$) states increases the RMSD(5-atom), RMSD(8-atom), and RMSD(all) values by only 0.02, 0.01, and 0.01 Å, respectively. The O1−O2, Fe−N(His384), Cu−O2, and especially Fe−O1 bond lengths/distances in av-*xyz*(1) agree with the observed values in 3S8G.pdb very well. Therefore, it is also likely that the observed X-ray crystal structure is a mixture of these four states.

In case 2, when we mix all six Fe^{2+}−(O−OH)$^-$−Cu^+(Y237$^-$) and Fe^{2+}−(HO−O)$^-$−Cu^+(Y237$^-$) clusters equally together, the RMSD(5-atom), RMSD(8-atom), and RMSD(all) values of av-*xyz*(2) are 0.03, 0.05, and 0.02 Å larger than the corresponding av-*xyz* values of the three Fe^{2+}−(HO−O)$^-$−Cu^+(Y237$^-$) structures given in Table 7. Although these RMSD values for av-*xyz*(2) are still relatively small compared with the RMSD's of the av-*xyz* structures in Tables 1−4 and 6, the overall structural features of av-*xyz*(2) do not agree well with the experiment. The Fe−N(His384) distance (2.35 Å) of av-*xyz*(2) is 0.13 Å longer than the observed value (2.22 Å). As mentioned before, in the X-ray crystal structure of 3S8G, the distance Cu−O2 (2.25 Å) is 0.14 Å shorter than Fe−O1 (2.39 Å), whereas in av-*xyz*(2), Fe−O1 (2.28 Å) is 0.33 Å shorter than Cu−O2 (2.61 Å). Therefore, even though $Fe^{2+,IS}$−(O−OH)$^-$−Cu^+(Y237$^-$) and $Fe^{2+,HS}$−(O−OH)$^-$−Cu^+(Y237$^-$) may coexist with the other four states, they are the minority in the radiation-reduced crystals.

4.5. Fe^{2+}−HOOH−Cu^+ DNC Calculations. Finally, to see if H_2O_2 represents the O1−O2 dioxygen species in the DNC of the 3S8G X-ray crystal structure, we have performed geometry optimization calculations for the Fe^{2+}−HOOH−Cu^+ cluster (see Figure 7 for the starting geometry of the DNC) in the following three spin states: $Fe^{2+,LS}$−HOOH−Cu^+, $Fe^{2+,IS}$−HOOH−Cu^+, and $Fe^{2+,HS}$−HOOH−Cu^+. During geometry optimizations, the O1−O2 bond in all three states broke, and the final states $Fe^{3+,LS}$−OH^-···OH^-−Cu^{2+}(AF), $Fe^{3+,LS}$−OH^-···OH^-−Cu^{2+}(F), and $Fe^{3+,IS}$−OH^-···OH^-−Cu^{2+}(F) were obtained, respectively. Therefore, Fe^{2+}−HOOH−Cu^+ is not likely to be a stable state, and the O1−O2 dioxygen species in the X-ray crystal structure is not H_2O_2.

4.6. Formation and Stability of the Metal-Bound HO_2^- Species. Relevant but difficult questions arise about the HO_2^- presence in the active site:

(1) How is the HO_2^- formed within the active site in the DNC of the C*c*O X-ray crystal structure?
(2) What factors account for its stability there?
(3) Why does the HO_2^- not react further, as the peroxo species in the normal catalytic cycle does?

Tiefenbrunn et al.[42] have pointed out that, in the high-energy X-ray (12 keV) beam, H$^\bullet$ and HO$^\bullet$ radicals are produced from water radiolysis and subsequently aquated electrons from H$^\bullet$ radicals, which can reduce the Fe and Cu sites. Further, they have suggested[42] that a bridging O1−O2 peroxide "might arise from the recombination (2 HO$^\bullet$ → H_2O_2) of two radiation produced HO$^\bullet$ radicals formed either very near to or even in the space between the two metals of the active site". As a related but distinct alternative, direct rapid X-ray photoabsorption by the H_2O and OH^- binding between Fe^{3+} and Cu^{2+} can lead to reduction of the metals by photoelectrons, highly excited bound electrons, and Auger electrons. This photoreaction will lead also to a cationic H_2O^+ and a HO$^\bullet$ radical with excess protons in the space with positive electrostatic potential (ESP) between Fe^{2+} and Cu^+. The positive ESP will promote deprotonation with formation and stabilization of anions such as HO_2^-. At low temperature under liquid nitrogen, the trapped HO_2^- species may have a binding geometry above the global energy minimum.

In the normal catalytic cycle, the expected peroxide intermediate is Fe^{3+}−O_2^{2-}−Cu^{2+}, which is highly transient, so that only states later in the catalytic cycle are observed. Consistently, our structural comparisons between the calculated

dx.doi.org/10.1021/ic401858s | Inorg. Chem. 2013, 52, 14072−14088

$Fe^{3+}-O_2^{2-}-Cu^{2+}$ geometry and the experimental X-ray structure are not in good agreement (see Table 1), and the structural match with $Fe^{2+}-(HO-O)^{-}-Cu^{+}$ is much better (Tables 5, 7 and 8). The latter state is too electron rich to proceed along the normal catalytic cycle pathway, which involves high-oxidation-state intermediates $[Fe^{4+}{=}O]^{2+}$, Cu^{2+}, and tyrosine (Tyr237) radical. At the same time, this species lacks one proton in comparison to HOOH, which reacts quickly to reverse the catalytic cycle in the presence of reduced Fe^{2+} and Cu^{+} (hydrogen peroxide shunt or short circuit).[70,71] We have calculated direct cleavage and reduction of H_2O_2 (section 4.5), a result also consistent with experimental observation of the "resting" oxidized state **O** (Fe^{3+},Cu^{2+}) when H_2O_2 is introduced to the reduced Fe^{2+},Cu^{+} state in bovine C*c*O.[70,71] The additional intermediate $Fe^{4+}{=}O$,Cu^{+} (intermediate **F**′) is also seen experimentally (by flow-flash kinetics followed by optical spectroscopy), which converts to **O**. The exact character of **O** is not yet known, but a form such as $Fe^{3+}-OH^{-}\cdots H_2O-Cu^{2+}$ or Fe^{3+}-$H_2O\cdots OH^{-}-Cu^{2+}$ is probable.

In contrast to Kaila et al.[41] and in agreement with Kieber-Emmons (and many others),[29,30] we think that it is very unlikely that molecular O_2 is bound to the resting oxidized $Fe^{3+}\cdots Cu^{2+}$ state of the DNC, on the basis of the expected weak affinity for Fe^{3+} and spectroscopic observations. This implies that the hydroperoxide type species seen in the X-ray structure probably does not originate from the native reactant O_2, given that the radiolytic reduction by the X-ray beam occurs after the crystal is flash-frozen in liquid nitrogen.[42] Under these conditions, diffusion of O_2 (or HO_2^{-} anion) from the oxygen entry channel[72−74] into the space directly between the $Fe^{2+}\cdots Cu^{+}$ would be difficult, particularly since H_2O and/or OH^{-} present there would need to be displaced. Liu et al.[37] found that when C*c*O in *Tt* is chemically reduced prior to freezing in liquid nitrogen, the space between Fe^{2+} and Cu^{+} is empty, but when radiolytic reduction in the X-ray beam is employed after freezing in liquid nitrogen, there is one OH^{-} or H_2O between Fe^{2+} and Cu^{+}. Also, the lipidic cubic phase X-ray structure of Tiefenbrunn et al.[42] exhibits a larger number of ordered water molecules in the protein interior than in the earlier structures[32,33,37] crystallized from ba_3 protein solubilized in detergent micelles. This higher water occupancy in the lipidic cubic phase crystals strengthens the argument against O_2 exchange for H_2O or OH^{-} between $Fe^{2+}\cdots Cu^{+}$ within the frozen crystal.

A recent resonance Raman study on the resting oxidized state of bovine heart C*c*O has shown a feature at 755 cm^{-1} (upon 647.1 nm excitation), which was assigned to an intraperoxide (O_2^{2-}) stretch (ν_{O-O}) on the basis of its disappearance upon exposure to cyanide.[40] However, a ligand−metal (ν_{Fe-O}) mode is not present in the spectrum (400−1200 cm^{-1}), and an isotope labeling (^{18}O) study has not been reported.[29] Kieber-Emmons et al. have reported the resonance Raman spectrum for the heme-peroxo-copper adduct $\{[(F_8)Fe(DCHIm)]$-O_2-$[Cu(AN)]\}^{+}$, in which O_2^{2-} bridges the metals in a μ-1,2 configuration.[29,30] They have found that the ν_{O-O} intraperoxide stretching mode is at 796 cm^{-1}, which is much higher than 755 cm^{-1}. This 755 cm^{-1} band also cannot represent the $Fe^{3+}-HOO^{-}-Cu^{2+}$ state. In note 31 of ref 29, Kieber-Emmons et al. indicated that the typical Cu−OOH intraperoxide stretching frequencies are more than 820 cm^{-1}. Further, in time-resolved resonance Raman experiments on ba_3 C*c*O from *T. thermophilus*, Egawa et al. found no oxygen-sensitive resonance Raman bands with $^{16}O_2-^{18}O_2$ substitution.[75]

5. CONCLUSIONS

Using OLYP potential, we have performed geometric and energetic calculations on the $Fe_{a3}\cdots O1-O2\cdots Cu_B$ DNC of the X-ray crystal structure (PDB code 3S8G)[42] of ba_3 C*c*O from *Thermus thermophilus*, to study whether the dioxygen O1−O2 species is O_2^{2-}, $O_2^{\bullet-}$, HO_2^{-}, or H_2O_2. Our calculations indicate that the O1−O2 observed in the DNC of the X-ray crystal structure is best represented by HO_2^{-}. Further, in comparison with the X-ray crystal structure, the Tyr237 side chain is better described as the deprotonated $Tyr237^{-}$ anion form. It is likely that the $Tyr237^{-}$ form is caused by the X-ray radiation and/or by the low temperature, which could inhibit proton transfer from the K-path to the DNC.

When the proton of the HO_2^{-} is on atom O1 (which is closer to Fe, see Figures 5, 11, and 12), on the basis of the calculated electronic energies, we cannot exclude the possibility that the three $Fe^{2+,LS}-(HO-O)^{-}-Cu^{+}(Y237^{-})$, $Fe^{2+,IS}-(HO-O)^{-}-Cu^{+}(Y237^{-})$, and $Fe^{2+,HS}-(HO-O)^{-}-Cu^{+}(Y237^{-})$ states may coexist (Table 7). Then the structure of the DNC in the 3S8G X-ray crystal structure represents the superposition of the conformations of these three states. We have calculated the average (av-*xyz*) of the Cartesian coordinates of the optimized geometries of these three clusters and obtained very small RMSD's in comparison with the X-ray crystal structure (Table 7 and Figure 13).

When the proton of the HO_2^{-} is on atom O2 (which is closer to Cu; see Figures 6, 9, and 10), although the calculated electronic energies of the $Fe^{2+,LS}-(O-OH)^{-}-Cu^{+}(Y237^{-})$, $Fe^{2+,IS}-(O-OH)^{-}-Cu^{+}(Y237^{-})$, and $Fe^{2+,HS}-(O-OH)^{-}-Cu^{+}(Y237^{-})$ states (see Table 6) are all lower than the energies of the $Fe^{2+,LS}-(HO-O)^{-}-Cu^{+}(Y237^{-})$, $Fe^{2+,IS}-(HO-O)^{-}-Cu^{+}(Y237^{-})$, and $Fe^{2+,HS}-(HO-O)^{-}-Cu^{+}(Y237^{-})$ states (Table 7), none of the individual structures of the $Fe^{2+,LS}-(O-OH)^{-}-Cu^{+}(Y237^{-})$, $Fe^{2+,IS}-(O-OH)^{-}-Cu^{+}(Y237^{-})$, and $Fe^{2+,HS}-(O-OH)^{-}-Cu^{+}(Y237^{-})$ states or the superposition of these three states is consistent with the DNC structure observed in the X-ray crystal structure. However, the mixture of the $Fe^{2+}-(O-OH)^{-}-Cu^{+}(Y237^{-})$ states, especially the $Fe^{2+,LS}-(O-OH)^{-}-Cu^{+}(Y237^{-})$ state, with the three $Fe^{2+}-(HO-O)^{-}-Cu^{+}(Y237^{-})$ states still agrees well with the experiment. Therefore, if the 3S8G X-ray crystal structure is represented by the superposition of the $Fe^{2+}-(HO-O)^{-}-Cu^{+}(Y237^{-})$ and $Fe^{2+}-(O-OH)^{-}-Cu^{+}(Y237^{-})$ states, the majority of the crystals were likely structurally trapped in the $Fe^{2+}-(HO-O)^{-}-Cu^{+}(Y237^{-})$ states at low temperature, and a minority were in the $Fe^{2+}-(O-OH)^{-}-Cu^{+}(Y237^{-})$ states (mainly in the $Fe^{2+,LS}-(O-OH)^{-}-Cu^{+}(Y237^{-})$ state).

After additional exploration, we also found some local minima of the $Fe^{2+,LS}-(HO-O)^{-}-Cu^{+}(Y237^{-})$ state, for instance $Fe^{2+,LS}-(HO-O)^{-}-Cu^{+}(Y237^{-})^{(3)}$ (Table 8, and Figure 14), which has a much longer Fe···Cu distance but is only ∼2.6 kcal mol^{-1} higher in energy than the lowest-energy structure ($Fe^{2+,LS}-(HO-O)^{-}-Cu^{+}(Y237^{-})$ in Table 7, also labeled as $Fe^{2+,LS}-(HO-O)^{-}-Cu^{+}(Y237^{-})^{(1)}$ in Table 8). This calculated structure yields very similar structural features around the Fe···O1−O2···Cu DNC to the X-ray crystal structure. Therefore, if the experimentally observed structure represents a single state but not a mixture, it is then likely to be in the $Fe^{2+,LS}-(HO-O)^{-}-Cu^{+}(Y237^{-})$ state trapped near the $Fe^{2+,LS}-(HO-O)^{-}-Cu^{+}(Y237^{-})^{(3)}$ local minimum.

In our earlier paper on the catalytic reaction cycle for O_2 reduction−protonation and proton pumping,[11] we found that

dx.doi.org/10.1021/ic401858s | *Inorg. Chem.* 2013, 52, 14072−14088

the Tyr237$^-$ state was critically important for many steps of the catalytic cycle, including both proton uptake from the K-path and proton advancement to other tautomeric sites within the DNC. A number of groups have made similar proposals[2,6,76] supported by DFT calculations.

Although Fe^{2+}−HO_2^-−Cu^+ is not a physiological state, in general, these DFT structures, energies, and spin states provide a set of useful models for comparison with future high-resolution X-ray structures and with experimental spectroscopy on cytochrome *c* oxidases.

■ ASSOCIATED CONTENT

Ⓢ Supporting Information

Tables giving Cartesian coordinates of the OLYP optimized clusters discussed in Tables 1−8. This material is available free of charge via the Internet at http://pubs.acs.org.

■ AUTHOR INFORMATION

Corresponding Author

*L.N.: e-mail, lou@scripps.edu; tel, (858) 784-2840.

Notes

The authors declare no competing financial interest.

■ ACKNOWLEDGMENTS

This paper is dedicated to the memory of Jim Fee, who made critical contributions to the cytochrome *c* oxidase field and to the biochemistry of metalloenzymes over the last 40 years. The ever-active, ever-inquiring Prof. J. A. Fee will be sorely missed by all his friends and co-workers. We are grateful for valuable discussions with Drs. C. David Stout, Andreas W. Götz, Ross C. Walker, Victoria A. Roberts, and Vijay S. Reddy. We thank The Scripps Research Institute for computational resources and the NIH for financial support (R01 GM100934). We are also grateful for the computer time that was provided by the San Diego Supercomputer Center through National Science Foundation award TG-CHE130010.

■ REFERENCES

(1) Richter, O. M. H.; Ludwig, B. *Rev. Physiol. Biochem. Pharmacol.* **2003**, *147*, 47−74.
(2) Babcock, G. T.; Wikström, M. *Nature* **1992**, *356*, 301−309.
(3) Ferguson-Miller, S.; Babcock, G. T. *Chem. Rev.* **1996**, *96*, 2889−2907.
(4) Malmström, B. G. *J. Biol. Inorg. Chem.* **1998**, *3*, 339−343.
(5) Nicholls, D. G.; Ferguson, S. J. *Bioenergetics 3*; Academic Press: San Diego, CA, 2002.
(6) Wikström, M. *Biochim. Biophys. Acta* **2012**, *1817*, 468−475.
(7) Kaila, V. R. I.; Verkhovsky, M. I.; Wikström, M. *Chem. Rev.* **2010**, *110*, 7062−7081.
(8) Konstantinov, A. A. *FEBS Lett.* **2012**, *586*, 630−639.
(9) von Ballmoos, C.; Adelroth, P.; Gennis, R. B.; Brzezinski, P. *Biochim. Biophys. Acta* **2012**, *1817*, 650−657.
(10) Farver, O.; Chen, Y.; Fee, J. A.; Pecht, I. *FEBS Lett.* **2006**, *580*, 3417−3421.
(11) Fee, J. A.; Case, D. A.; Noodleman, L. *J. Am. Chem. Soc.* **2008**, *130*, 15002−15021.
(12) Chance, B.; Saronio, C.; Leigh, J. S. *Proc. Natl. Acad. Sci. U.S.A.* **1975**, *72*, 1635−1640.
(13) Varotsis, C.; Woodruff, W. H.; Babcock, G. T. *J. Am. Chem. Soc.* **1989**, *111*, 6439−6440.
(14) Han, S.; Ching, Y. C.; Rousseau, D. L. *Proc. Natl. Acad. Sci. U.S.A.* **1990**, *87*, 2491−2495.
(15) Ogura, T.; Takahashi, S.; Shinzawaitoh, K.; Yoshikawa, S.; Kitagawa, T. *J. Am. Chem. Soc.* **1990**, *112*, 5630−5631.
(16) Oliveberg, M.; Brzezinski, P.; Malmstrom, B. G. *Biochim. Biophys. Acta* **1989**, *977*, 322−328.
(17) Wikström, M. *Proc. Natl. Acad. Sci. U.S.A.* **1981**, *78*, 4051−4054.
(18) Weng, L. C.; Baker, G. M. *Biochemistry* **1991**, *30*, 5727−5733.
(19) Kitagawa, T.; Ogura, T. *Prog. Inorg. Chem.* **1997**, *45*, 431−479.
(20) Ogura, T.; Kitagawa, T. *Biochim. Biophys. Acta* **2004**, *1655*, 290−297.
(21) Proshlyakov, D. A.; Pressler, M. A.; Babcock, G. T. *Proc. Natl. Acad. Sci. U.S.A.* **1998**, *95*, 8020−8025.
(22) Fabian, M.; Wong, W. W.; Gennis, R. B.; Palmer, G. *Proc. Natl. Acad. Sci. U.S.A.* **1999**, *96*, 13114−13117.
(23) Zimmermann, B. H.; Nitsche, C. I.; Fee, J. A.; Rusnak, F.; Munck, E. *Proc. Natl. Acad. Sci. U.S.A.* **1988**, *85*, 5779−5783.
(24) Fann, Y. C.; Ahmed, I.; Blackburn, N. J.; Boswell, J. S.; Verkhovskaya, M. L.; Hoffman, B. M.; Wikstrom, M. *Biochemistry* **1995**, *34*, 10245−10255.
(25) Blomberg, L. M.; Blomberg, M. R. A.; Siegbahn, P. E. M. *Biochim. Biophys. Acta* **2006**, *1757*, 31−46.
(26) Siegbahn, P. E. M.; Blomberg, M. R. A. *J. Phys. Chem. A* **2008**, *112*, 12772−12780.
(27) Blomberg, M. R. A.; Siegbahn, P. E. M. *Biochim. Biophys. Acta* **2012**, *1817*, 495−505.
(28) Lee, H. J.; Reimann, J.; Huang, Y. F.; Adelroth, P. *Biochim. Biophys. Acta* **2012**, *1817*, 537−544.
(29) Kieber-Emmons, M. T.; Qayyum, M. F.; Li, Y. Q.; Halime, Z.; Hodgson, K. O.; Hedman, B.; Karlin, K. D.; Solomon, E. I. *Angew. Chem., Int. Ed.* **2012**, *51*, 168−172.
(30) Kieber-Emmons, M. T.; Li, Y. Q.; Halime, Z.; Karlin, K. D.; Solomon, E. I. *Inorg. Chem.* **2011**, *50*, 11777−11786.
(31) Chang, H. Y.; Choi, S. K.; Vakkasoglu, A. S.; Chen, Y.; Hemp, J.; Fee, J. A.; Gennis, R. B. *Proc. Natl. Acad. Sci. U.S.A.* **2012**, *109*, 5259−5264.
(32) Soulimane, T.; Buse, G.; Bourenkov, G. P.; Bartunik, H. D.; Huber, R.; Than, M. E. *EMBO J.* **2000**, *19*, 1766−1776.
(33) Hunsicker-Wang, L. M.; Pacoma, R. L.; Chen, Y.; Fee, J. A.; Stout, C. D. *Acta Crystallogr., Sect. D: Biol. Crystallogr.* **2005**, *61*, 340−343.
(34) Ostermeier, C.; Harrenga, A.; Ermler, U.; Michel, H. *Proc. Natl. Acad. Sci. U.S.A.* **1997**, *94*, 10547−10553.
(35) Qin, L.; Hiser, C.; Mulichak, A.; Garavito, R. M.; Ferguson-Miller, S. *Proc. Natl. Acad. Sci. U.S.A.* **2006**, *103*, 16117−16122.
(36) Yoshikawa, S.; Shinzawa-Itoh, K.; Nakashima, R.; Yaono, R.; Yamashita, E.; Inoue, N.; Yao, M.; Fei, M. J.; Libeu, C. P.; Mizushima, T.; Yamaguchi, H.; Tomizaki, T.; Tsukihara, T. *Science* **1998**, *280*, 1723−1729.
(37) Liu, B.; Chen, Y.; Doukov, T.; Soltis, S. M.; Stout, C. D.; Fee, J. A. *Biochemistry* **2009**, *48*, 820−826.
(38) Aoyama, H.; Muramoto, K.; Shinzawa-Itoh, K.; Hirata, K.; Yamashita, E.; Tsukihara, T.; Ogura, T.; Yoshikawa, S. *Proc. Natl. Acad. Sci. U.S.A.* **2009**, *106*, 2165−2169.
(39) Koepke, J.; Olkhova, E.; Angerer, H.; Muller, H.; Peng, G. H.; Michel, H. *Biochim. Biophys. Acta* **2009**, *1787*, 635−645.
(40) Sakaguchi, M.; Shinzawa-Itoh, K.; Yoshikawa, S.; Ogura, T. *J. Bioenerg. Biomembr.* **2010**, *42*, 241−243.
(41) Kaila, V. R. I.; Oksanen, E.; Goldman, A.; Bloch, D. A.; Verkhovsky, M. I.; Sundholm, D.; Wikström, M. *Biochim. Biophys. Acta* **2011**, *1807*, 769−778.
(42) Tiefenbrunn, T.; Liu, W.; Chen, Y.; Katritch, V.; Stout, C. D.; Fee, J. A.; Cherezov, V. *PLoS One* **2011**, *6*, e22348.
(43) Kim, E.; Chufan, E. E.; Kamaraj, K.; Karlin, K. D. *Chem. Rev.* **2004**, *104*, 1077−1133.
(44) Handy, N. C.; Cohen, A. J. *Mol. Phys.* **2001**, *99*, 403−412.
(45) Lee, C. T.; Yang, W. T.; Parr, R. G. *Phys. Rev. B* **1988**, *37*, 785−789.
(46) Vancoillie, S.; Zhao, H. L.; Radon, M.; Pierloot, K. *J. Chem. Theory Comput.* **2010**, *6*, 576−582.
(47) Radoń, M.; Pierloot, K. *J. Phys. Chem. A* **2008**, *112*, 11824−11832.

(48) *ADF Amsterdam Density Functional Software*, SCM, Theoretical Chemistry, Vrije Universiteit, Amsterdam, The Netherlands; http://www.scm.com.
(49) te Velde, G.; Bickelhaupt, F. M.; Baerends, E. J.; Guerra, C. F.; Van Gisbergen, S. J. A.; Snijders, J. G.; Ziegler, T. *J. Comput. Chem.* **2001**, *22*, 931−967.
(50) Guerra, C. F.; Visser, O.; Snijders, J. G.; te Velde, G.; Baerends, E. J., Parallelisation of the Amsterdam Density Functional Program. In *Methods and Techniques for Computational Chemistry*; Clementi, E., Corongiu, C., Eds.; STEF: Cagliari, Italy, 1995; pp 303−395.
(51) Klamt, A.; Schüürmann, G. *J. Chem. Soc., Perkin Trans. 2* **1993**, 799−805.
(52) Klamt, A. *J. Phys. Chem.* **1995**, *99*, 2224−2235.
(53) Klamt, A.; Jonas, V. *J. Chem. Phys.* **1996**, *105*, 9972−9981.
(54) Pye, C. C.; Ziegler, T. *Theor. Chem. Acc.* **1999**, *101*, 396−408.
(55) Han, W.-G.; Sandala, G. M.; Giammona, D. A.; Bashford, D.; Noodleman, L. *Dalton Trans.* **2011**, *40*, 11164−11175.
(56) Han, W.-G.; Noodleman, L. *Inorg. Chem.* **2011**, *50*, 2302−2320.
(57) Han, W.-G.; Noodleman, L. *Theor. Chem. Acc.* **2010**, *125*, 305−317.
(58) Han, W.-G.; Giammona, D. A.; Bashford, D.; Noodleman, L. *Inorg. Chem.* **2010**, *49*, 7266−7281.
(59) Han, W.-G.; Noodleman, L. *Dalton Trans.* **2009**, 6045−6057.
(60) Han, W.-G.; Noodleman, L. *Inorg. Chim. Acta* **2008**, *361*, 973−986.
(61) Han, W. G.; Liu, T. Q.; Lovell, T.; Noodleman, L. *J. Am. Chem. Soc.* **2005**, *127*, 15778−15790.
(62) Noodleman, L. *J. Chem. Phys.* **1981**, *74*, 5737−5743.
(63) Noodleman, L.; Case, D. A. *Adv. Inorg. Chem.* **1992**, *38*, 423−470.
(64) Noodleman, L.; Lovell, T.; Han, W.-G.; Liu, T.; Torres, R. A.; Himo, F., Density Functional Theory. In *Comprehensive Coordination Chemistry II, From Biology to Nanotechnology*; Lever, A. B., Ed.; Elsevier: Amsterdam, 2003; Vol. 2, pp 491−510.
(65) Götz, A. W. Personal communication, 2013. In very recent DFT calculations on the DNC models similar to Intermediate State 2 (reduced state R) of ref 11 containing 183 atoms, our coworker A. W. Götz found a large difference in the Tyr237-geranyl sidechain O···O distance depending on whether Tyr237 is neutral or an anion (charged H bond).
(66) Tissandier, M. D.; Cowen, K. A.; Feng, W. Y.; Gundlach, E.; Cohen, M. H.; Earhart, A. D.; Coe, J. V.; Tuttle, T. R. *J. Phys. Chem. A* **1998**, *102*, 7787−7794.
(67) Lewis, A.; Bumpus, J. A.; Truhlar, D. G.; Cramer, C. J. *J. Chem. Educ.* **2004**, *81*, 596−604.
(68) Lewis, A.; Bumpus, J. A.; Truhlar, D. G.; Cramer, C. J. *J. Chem. Educ.* **2007**, *84*, 934.
(69) Tawa, G. J.; Topol, I. A.; Burt, S. K.; Caldwell, R. A.; Rashin, A. A. *J. Chem. Phys.* **1998**, *109*, 4852−4863.
(70) Zaslavsky, D.; Smirnova, I. A.; Adelroth, P.; Brzezinski, P.; Gennis, R. B. *Biochemistry* **1999**, *38*, 2307−2311.
(71) Zaslavsky, D.; Smirnova, I. A.; Brzezinski, P.; Shinzawa-Itoh, K.; Yoshikawa, S.; Gennis, R. B. *Biochemistry* **1999**, *38*, 16016−16023.
(72) McDonald, W.; Funatogawa, C.; Li, Y.; Szundi, I.; Chen, Y.; Fee, J. A.; Stout, C. D.; Einarsdottir, O. *Biochemistry* **2013**, *52*, 640−652.
(73) Luna, V. M.; Fee, J. A.; Deniz, A. A.; Stout, C. D. *Biochemistry* **2012**, *51*, 4669−4676.
(74) Luna, V. M.; Chen, Y.; Fee, J. A.; Stout, C. D. *Biochemistry* **2008**, *47*, 4657−4665.
(75) Egawa, T.; Chen, Y.; Fee, J. A.; Yeh, S. R.; Rousseau, D. L. *Biochim. Biophys. Acta* **2012**, *1817*, 666−671.
(76) Himo, F.; Noodleman, L.; Blomberg, M. R. A.; Siegbahn, P. E. M. *J. Phys. Chem. A* **2002**, *106*, 8757−8761.

■ NOTE ADDED AFTER ASAP PUBLICATION

This paper was published on the Web on November 21, 2013, with minor text errors throughout the paper. The corrected version was reposted on November 27, 2013.